SPECTRAL ESTIMATION OF WAVE-DRIVEN FLUCTUATIONS IN RAYLEIGH LIDAR TEMPERATURE MEASUREMENTS

By

Sharma Nadakuditi

RECOMMENDED:

C. S. Gardner

Joseph S. Martin

Advisory Committee Chair

C. S. Gardner

Chair, Department of Electrical and Computer Engineering

APPROVED:

John Aspnes

Dean, College of Engineering and Mines

Susan McHarris

Dean of the Graduate School

April 26, 2005

Date

SPECTRAL ESTIMATION OF WAVE-DRIVEN FLUCTUATIONS IN RAYLEIGH LIDAR TEMPERATURE MEASUREMENTS

A

THESIS

Presented to the Faculty

of the University of Alaska Fairbanks

in Partial Fulfillment of the Requirements

for the Degree of

MASTER OF SCIENCE

By

Sharma Nadakuditi

Fairbanks, AK

May 2005

Abstract

The NICT-Rayleigh lidar has been operated at Chatanika, Alaska (65°N, 147°W) since November 1997. These lidar observations have yielded temperature and density measurements in the stratosphere and mesosphere (~40-80 km). The goal of this thesis is to estimate the signal and noise power in the relative temperature perturbations. The uncertainties in these estimates due to instrumental variability and geophysical variability are also determined. This analysis quantifies the relative contributions of gravity waves and instrumental noise to the total power measured by the lidar. Eighty-nine nights of observations have yielded 80 sets of data that are of sufficient quality to study the gravity-wave activity at 30-minute resolution in the 40-50 km altitude region. The rms temperature and density perturbations from early August to mid-May are found to be statistically identical. The rms temperature fluctuations are found to have an average value of 0.44% with a maximum value of 1.28% on March 12th 2004 and a minimum value of 0.20% on September 16th 2003. These rms amplitudes are similar to values reported from other Arctic sites.

Table of Contents

List of Figures

List of Tables

Acknowledgements

I thank Dr. Richard Collins for his advice during my graduate studies and his guidance in preparing this thesis. I also thank him for providing me with a graduate assistantship at the University of Alaska Fairbanks. I thank Dr. Joseph Hawkins and Dr. Vikas Sonwalkar for serving on my graduate committee and providing helpful suggestions. I thank Justin Breese, Laura Cutler, Keith Nowicki, Weiyuan Wang, Tim Stern, Manasi Peshave, Jia Yue, Liguo Su and Brentha Thurairajah for helping me in making the lidar measurements. I thank the staff of PFRR (Poker Flat Research Range) for the support of the lidar facility at PFRR. I thank Dr. Kohei Mizutani and NICT (National Institute of Information and Communications Technology) for supporting the Rayleigh lidar program at PFRR. I would finally like to acknowledge the support of the NSF CEDAR (Coupling, Energetics and Dynamics of Atmospheric Regions) program.

Dedication

To my mother, father, sister and friends.

Chapter 1. Introduction

Section 1.1: The Middle Atmosphere

The middle atmosphere extends from approximately 10 to 100 km. Interest in the middle atmosphere has increased since the discovery of the "ozone hole" in the Antarctic stratosphere in 1980 (see review article by Solomon [1999] and references therein). The temperature structure of the atmosphere is illustrated in Figure 1.1. The temperature profile in Figure 1.1 is taken from the Mass Spectrometer-Incoherent Scatter Extended 1990 model (MSISE-90) of Hedin and co-workers [Hedin, 1991]. Initially, the atmosphere cools with altitude from the surface of the Earth to about 10 km. This lowest region is called the troposphere. At altitudes above 10 km the atmosphere warms with altitude up to about 50 km. This region is called the stratosphere. The atmosphere then cools with altitude up to 90 or 100 km. This region is called the mesosphere. Finally, above the mesosphere the atmosphere warms with altitude. This region is called the thermosphere. The stratosphere, mesosphere and lower thermosphere are collectively termed the middle atmosphere. The warming of the atmosphere in the stratosphere is due to absorption of ultraviolet solar radiation (~240-290 nm) by the ozone layer. The warming in the thermosphere is due to absorption of extreme ultraviolet radiation (< 100 nm) [e.g., Wayne, 1985]. As we would expect, the temperature at the surface of the Earth is warmer in summer than winter. In fact the summertime temperature profile is warmer than the wintertime profile up to about 70 km. The general temperature structure is well understood in terms of radiative transfer and solar absorption by ozone and the atmosphere is said to be in radiative equilibrium (e.g., Brasseur and Solomon, [1984]; Andrews et al., [1987]). However, in the upper mesosphere (~70 to 90 km) the wintertime atmosphere is significantly warmer than the summertime atmosphere and is not in radiative equilibrium.

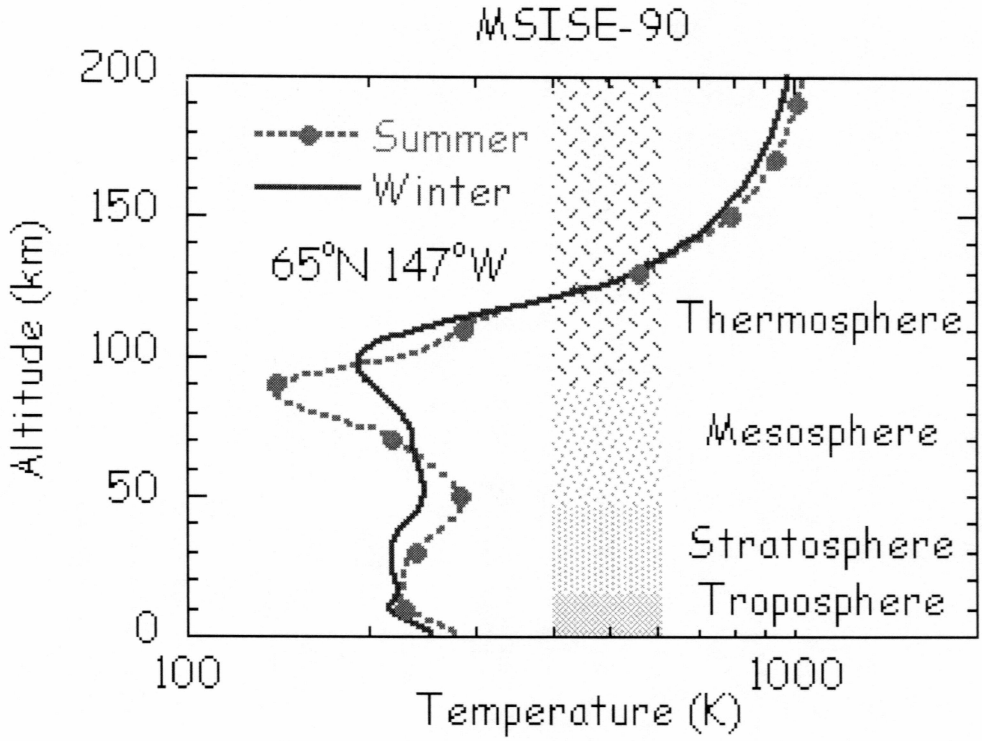

Figure 1.1: The temperature profile for the atmosphere at Chatanika, Alaska (65°N, 147°W). The data are taken from the MSISE-90 model of Hedin and co-workers [Hedin, 1991]. The summer data (dotted and dashed line) are for midnight on June 21, 2002. The winter data (solid) are for midnight on December 21, 2001. The shaded column shows the division of the atmosphere into the troposphere, stratosphere, mesosphere, and thermosphere (from Wang [2003]).

This departure from radiative equilibrium is understood to arise from wave effects in the atmosphere (see recent reviews by Holton and Alexander [2000] and Fritts and Alexander [2003] and references therein). Gravity waves are small-scale (i.e., horizontal wavelengths of ~100-1000 km) waves that result from the balance of inertia and buoyancy forces. Gravity waves are generated from small-scale disturbances (~100 km) in the atmosphere such as wind flow over mountains and storms. These waves propagate upward in the atmosphere, and then break and produce an acceleration of the zonal flow. The resulting forcing tends to decelerate the mean zonal flow in both the summer and winter hemispheres and gives rise to a pole-to-pole meridional circulation cell that has rising motion over the summer pole (resulting in cooling) and descending motion over the winter pole (resulting in warming). The summer cooling dominates over radiative heating and the summertime mesopause temperatures fall to ~120 K. This is ~80 K colder than expected from radiative forcing alone. The winter heating dominates over radiative cooling and the winter time mesopause temperatures rise to ~200 K. This is ~80 K warmer than expected from radiative forcing alone. Given the contribution of these small-scale waves to the large-scale circulation, the goal of observational gravity wave studies has been to characterize the waves so that they can be parameterized in large-scale circulation models. The mean square and root-mean-square amplitudes of the wave-induced fluctuation quantities (e.g., rms wind, rms temperature, rms density fluctuations) are used to quantify the energy or power in the wave fields. These quantities are widely used to quantify the gravity wave activity in the middle atmosphere.

Section 1.2: Rayleigh Lidar

Studies of the middle atmosphere have been difficult due to technical limitations in instrumentation. Meteorological balloons reach altitudes of up to 30 km. Above 30 km the balloons pop, thereby preventing measurements at higher altitudes. Radar systems can only make measurements up to about 30 km or above 60 km, due to the lack of scattering media (i.e., water molecules and electrons) in the middle atmosphere.

Airglow measurements are confined to the naturally luminous layers above 80 km. Rockets provide intermittent measurements during campaign periods and are expensive to launch. Satellites orbit far above the mesosphere (>1000 km) and make measurements over scales that cannot resolve gravity wave motions. So, there is a region from about 30 km to 80 km where there are relatively few routine measurements being made. Rayleigh lidar systems are so named because they measure the Rayleigh scatter from air molecules [Lord Rayleigh, 1871]. Thus, in an atmosphere free of clouds and aerosols, the lidar signal is proportional to the density of the atmosphere. A lidar type approach, involving a searchlight, was first proposed in 1930 by Synge [Synge, 1930]. In 1951, Elterman implemented one of the first Rayleigh lidar-type systems that could reach the stratosphere by using a searchlight to measure the stratospheric density distribution (10-70 km) [Elterman, 1951]. The first experimental Rayleigh lidar using a laser was demonstrated in 1970 [Kent and Wright, 1970]. A systematic approach was later developed by Hauchecorne and co-workers, which showed improved accuracy over the earlier approach [Hauchecorne and Chanin, 1987]. Currently, Rayleigh lidars are widely used in studies of the middle atmosphere, particularly in the altitude range of 30 km to 80 km, which is aerosol free. Long-term observations have been ongoing at the Observatoire de Haute Provence (OHP) in France (44°N, 6°E) and at the Jet Propulsion Laboratory (JPL) Table Mountain Facility (TMF) in the United States (34.4°N, 117.7°W) [LeBlanc et al., 1998]. These observations have yielded studies of long-term trends as well as short-term waves and tides [e.g., LeBlanc and Hauchecorne, 1997]. A highlight of the OHP observations is the detection of a statistically significant long-term temperature trend in the stratosphere and mesosphere. Analysis of the data set has yielded a cooling of 0.4 K/year in the mesosphere and 0.1 K/year in the stratosphere over a near 20-year period from 1979 to 1994 [Keckhut et al., 1995]. Short-term observations at Eureka, Canada (80°N, 86°W) have been made during winter and spring to study the thermal structure of the polar stratospheric vortex [Duck et al., 2000]. This study has yielded insight into the

coupling between radiative and dynamic processes in the circulation of the middle atmosphere.

Rayleigh lidar systems typically employ powerful Nd:YAG lasers that are technologically mature and can be maintained and operated in a routine fashion [e.g., Hecht, 1992]. The receiver does not require wavelength tuning, so while daytime measurements require precise design (very narrow band pass filtering around 532 nm to avoid counting sunlight), nighttime measurements are relatively straightforward. The only physical assumption concerning the method is that the atmosphere is in hydrostatic equilibrium, which is valid over the temporal (several hours) and spatial (several km) scales of the measurement [Chanin, 1984]. The other successful lidar technique for measuring middle atmosphere temperature is the Na-resonance Doppler temperature lidar that uses the hyperfine structure of Na atoms in the mesopause region (80-100 km) to determine the wind and temperature [Bills et al., 1991]. Currently, Rayleigh lidar measurements remain the only viable ground-based technique for routinely measuring stratospheric and mesospheric temperature profiles.

Section 1.3: The NICT–Rayleigh Lidar at Poker Flat Research Range

The National Institute of Information and Communications Technology (NICT) of Tokyo, Japan installed a Rayleigh lidar (light detecting and ranging) system at Poker Flat Research Range (PFRR), Chatanika, Alaska (65° N, 147° W) in November 1997. The Rayleigh lidar was installed by staff from the NICT as part of a collaborative effort between the Geophysical Institute (GI) and the NICT [Mizutani et al., 2000; Cutler 2000]. The Rayleigh lidar has been operated routinely since 1997 with a gap from January to August of 2001. From November 1997 to May 1999, the NICT–Rayleigh lidar operated in the Optics Facility at PFRR. From May 1999 to April 2000, it operated in the Davis Science Center at PFRR. Since August 2000 the lidar has operated at the new Lidar Research Laboratory at PFRR. In January 2001 the lidar receiver was

upgraded to allow simultaneous and independent Rayleigh lidar measurements at 532 nm and resonance lidar measurements at 372 nm. Measurements are taken frequently during the fall, winter and spring months, but less frequently during June and July due to the fact that PFRR is located near the Arctic Circle and does not experience astronomical darkness in summer. During fall, winter and spring the Rayleigh lidar observations have yielded measurements of the temperature profile from 40 to 80 km with 2 hour resolution sufficient to study the formation of mesospheric inversion layers [Cutler et al., 2001]. Observations in August have yielded measurements of noctilucent (or polar mesospheric) clouds [Collins et al., 2003]. In this study, we analyse 89 sets of nighttime observations that were made between November 14-15, 1997 and May 12-13, 2004. The observations were conducted during fall, winter and spring (i.e., August through mid-May).

The current configuration of the NICT–Rayleigh lidar is tabulated in Table 1.1. A detailed schematic diagram of the NICT–Rayleigh lidar system is shown in Figure 1.2. The NICT–Rayleigh lidar transmitter consists of a laser, a laser beam expander (LBE), a beam steering mirror (BSM), and a laser pulse detector (LPD). The NICT system laser is an Nd:YAG Continuum® Powerlite 8000 laser which emits at a wavelength of 532 nm. The laser is a typical Nd:YAG laser and has a Q-switched oscillator section followed by an amplifier, operating at 1064 nm and a second harmonic generator that generates the output light at 532 nm (for a standard description of Nd:YAG lasers see Silfvast [1996]). The laser beam transmitted by the Nd:YAG laser is expanded a factor of 10 by the laser beam expander. Then, the beam steering mirror reflects this beam upward into the sky. The alignment of the laser beam and the receiver telescope is maintained by examining the lidar echo from 60 km to 65 km to ensure that the beam falls within the telescope field-of-view (FOV) which is typically 1 mrad.

The NICT–Rayleigh receiver consists of a telescope, a beam splitter (BS), a interference filter (IF), a photomultiplier tube (PMT), a delay generator (DG), two high voltage power supplies (HVPS), a pre-amplifier (PA) a multi-channel scalar (MCS) unit and a computer. The laser echo from the sky is received by the Newtonian telescope. The

Table 1.1: Specifications of NICT–Rayleigh Lidar System at PFRR[1]

Transmitter	
Laser	Nd:YAG
Model	Continuum Powerlite 8020
Wavelength (λ_L)	532 nm
Repetition Rate (R_L)	20 Hz
Pulse Energy (E_L)	460 mJ
Pulse width	5-7 ns
Line width	1.0 cm^{-1}
Beam Expander	×10
Divergence	0.45 mrad
Receiver	
Telescope	Newtonian
Diameter	60 cm
Range Resolution	75 m
Optical Bandwidth	0.3 nm
Detector	Photomultiplier Tube
Model	Hamamatsu R3234-01
Preamplifier Gain	×5
Model	Stanford Research Systems SR445
Bandwidth	300 MHz
Digital Recorder	Multichannel Scalar
Model	Ortec Turbo MCS T914
Maximum Count Rate	150 MHz

1. Adapted from Wang [2003]

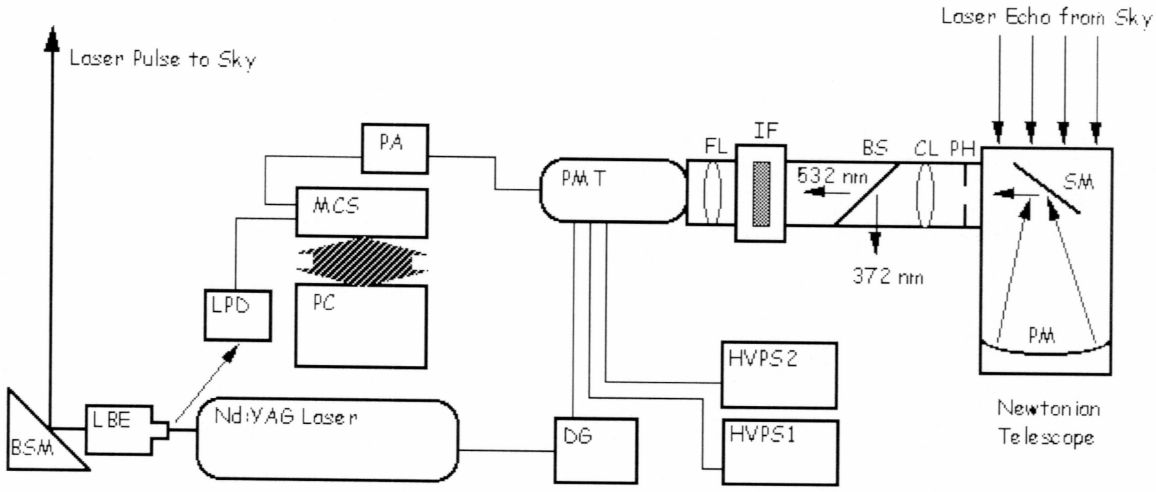

Figure 1.2: Schematic diagram of the NICT–Rayleigh lidar system at PFRR (from Wang [2003])

BS – Beam Splitter
CL – Collimating Lens
FL – Focusing Lens
IF – Interference Filter
LPD – Laser Pause Detector
PA – Pre-Amplifier
PH – Pin Hole
PMT – PhotoMultiplier Tube

BSM – Beam Steering Mirror
DG – Delay Generator
HVPS – High Voltage Power Supply
LBE – Laser Beam Expander
MCS – Multi-Channel Scalar
PC – Personal Computer
PM – Primary Mirror
SM – Secondary Mirror

backscattered photons are collected by the primary mirror (PM), reflected to the secondary mirror (SM), and then reflected toward the detector. The pinhole (PH) defines the telescope FOV by blocking light that enters the telescope at larger angles. After passing through the pinhole, the light is collimated by the collimating lens (CL). The beam splitter (BS) separates the incoming light into two wavelengths, 532 nm for Rayleigh lidar measurements and 372 nm for resonance lidar measurements. The collimated 532 nm light passes through an interference filter (IF) to eliminate any light at other wavelengths. The bandwidth of the interference filter is 0.3 nm. The photons are focused by the focusing lens onto the optical detector. The optical detector is a photomultiplier tube (PMT). The PMT is a sensitive, high-gain detector that converts single photons into electrical current pulses (for a standard description of PMTs see Skoog and Leary [1992]). The PMT is biased by a high voltage power supply (HVPS1) at -2000 V. A voltage of 200 V is applied to the first dynode of the PMT by a high voltage power supply (HVPS2) to reduce the gain of the PMT for the first 150 μs after the laser fires. The laser Q-switch signal triggers the delay generator (DG). The DG transmits a pulse of 150 μs duration (called a gate pulse) to the PMT. While the gate is applied to the PMT, the first dynode is biased by 200 V above its normal operating voltage and the gain of the PMT is reduced by over a factor of 10^6. The lidar echoes from altitudes below 22.5 km are detected at low gain while the higher altitude echoes are detected at the normal high gain. Thus, the detector avoids being overloaded by low-altitude signals. The current signal from the PMT is amplified by the pre-amplifier (PA) and then is transmitted to the MCS unit. The MCS unit is a high-speed counter that counts the incoming PMT pulses in a given time window at rates of up to 150 MHz. By successively counting the pulses in a sequence of time windows (or range bins), the MCS forms a profile in time. The round trip time, t, is converted to altitude, z, using the speed of light, c, as $z = 2 \times c \times t$. For a 75 m resolution profile, the time bins are 0.5 μs. The 5-7 ns duration of the Nd-YAG laser pulse results in a 0.75-1.05 m convolution of the lidar echo. The MCS typically records 4096 range bins and provides an echo profile from the

ground to approximately 300 km. The next laser pulse triggers the MCS and this new echo profile is added coherently to the previous one. This process continues for a predetermined number of laser shots (typically 2000) and yields a single raw data profile. The personal computer (PC) continually queries the MCS unit. The MCS unit informs the PC when the data profile is ready and the data a re transferred to the PC. The PC stores the profile and then initializes the MCS unit to begin a new profile on the next laser pulse.

Section 1.4: Scope of this Study

The goal of this study is to extend the earlier work of Cutler, Wang, and co-workers (Cutler, [2000]; Wang [2003]). Cutler et al., [2001] presented initial temperature measurements at PFRR and described the mesospheric inversion layers (MILs) that were observed. Wang [2003] examined the Rayleigh lidar inversion techniques to assess possible biases in the retrievals of both temperature and density profiles as well as relative density fluctuations. Wang employed statistical as well as spectral analysis techniques to quantify the signal and noise power contributions to the total measured power in the relative density fluctuations. In this study we examine the relative temperature perturbation profiles and study biases in the estimation of temperature fluctuations. We employ spectral analysis methods to examine the fluctuations and statistical techniques to estimate the signal power, noise power and uncertainties in their estimation. Duck and co-workers have used the relative temperature perturbations to study wave activity in the middle atmosphere [Duck et al., 2000]. Gerrard and co-workers have used the relative density perturbations to study wave activity [Gerrard et al., 1998]. A goal of this thesis is to determine if there are any differences in the wave activity determined from temperature and density perturbations. We compare the results for temperature and density perturbations to determine if there are any differences between them.

In Chapter 2, we present the derivation of relative temperature perturbations from the measured lidar temperature profiles. We also examine different processing methods

for determining the background temperature profile and its effect on the estimates of the relative temperature perturbations. In Chapter 3, we use spectral analysis to calculate the noise component in the total perturbation power and hence determine the signal component in the measurement. We also examine the effects of changes in time resolution of the data, smoothing of photon counts, and band limiting in space and time on the estimates of signal power. In Chapter 4, we compute the geophysical and instrumental uncertainties in the measurement of the signal power. In Chapter 5, we present gravity wave activity in terms of rms amplitude of relative temperature and relative density perturbations for 89 nights of observations. We compare the results obtained from temperature perturbations to those obtained by density perturbations. Finally, in Chapter 6, we present our conclusions and suggestions for further work.

Chapter 2. Determination of Temperature Perturbations

Section 2.1: Introduction

In this chapter we present the derivation of relative temperature perturbations from the measured lidar temperature profiles. We also examine the effects of the processing methods of the background temperature profile on the estimates of the relative temperature perturbations.

Cutler [Cutler, 2000] and Wang [Wang, 2003] have described the Rayleigh lidar technique and the NICT-Rayleigh lidar system at PFRR in detail. In summary, the laser transmits a pulse of light into the sky and the optical echo from the sky is detected with a telescope and converted into an electronic signal by a photomultiplier tube (PMT). The PMT converts single photons into electrical current pulses. The electrical pulses are counted by a high-speed recorder and the echo is stored as a function of time-of-flight. Knowing the speed of light, the altitude is calculated from the round trip time-of-flight. This process is repeated for a predetermined number (typically 1000-2000) of laser pulses and then the individual echoes are integrated by the high-speed recorder to yield a raw photon count profile. The raw photon count profile is then transferred from the recorder to the hard-disk of a computer.

As a case study, we consider the observations from the night of March 7-8, 2002. The first raw photon count profile was acquired at 1933 LST (LST = UT – 9 h) and the last photon count profile was acquired at 0608 LST. Each profile represents the integration of 2000 laser shots over 100 s. A total of 368 raw photon count profiles, corresponding to 736,000 laser shots, are acquired over the 10 h 35 min observation period. The integrated photon count profile for the entire observation period is plotted as a function of altitude in Figure 2.1. This photon count profile represents the integration of 368 raw photon count profiles.

The features of this photon count profile can be readily explained using the lidar equation [e.g., Cutler, 2000; Wang, 2003]. The expected photon count signal, N(z), from a given altitude range, $z \pm \Delta z/2$, in a time interval, Δt, is given by,

$$N(z) = N_s(z) + N_B + N_D \tag{2.1}$$

$$N_S(z) = K_{sys} \times \frac{\rho(z)}{(z - z_0)^2} \cdot \Delta t \cdot \Delta z \tag{2.2}$$

where, $N_s(z)$ is the photon count signal, N_B is the background skylight, N_D is the detector dark count, $\rho(s)$ is the molecular number density at altitude z (m^{-3}) and z_0 is the altitude of the lidar system. K_{sys} is the system constant given by,

$$K_{sys} = \eta T^2 \frac{E_L R_L \sigma_\pi^R A_T}{hc/\lambda_L} \tag{2.3}$$

where E_L (= 450 mJ) is the laser pulse energy, R_L (= 20 pps) is the laser pulse repetition rate, σ_π^R is the effective backscatter cross section (6.23×10^{-32} m^2/sr) at λ_L, A_T (= 0.283 m^2) is the area of the telescope, h is Planck's constant (6.63×10^{-34} J s), c is the speed of light (3.00×10^8 m/s), and λ_L is the laser wavelength (= 532 nm). The lidar signal between 22.5 and 80 km decreases exponentially with altitude and is proportional to the atmospheric density profile. Above 90 km the signal remains constant with altitude as the signal is dominated by background skylight (i.e., N_B) and dark emission signal from the detector (i.e., N_D). These signals are constant with altitude as they are constant in time. The low altitude signal is reduced by gain switching of the detector to avoid overloading of the receiver system by low-altitude echoes.

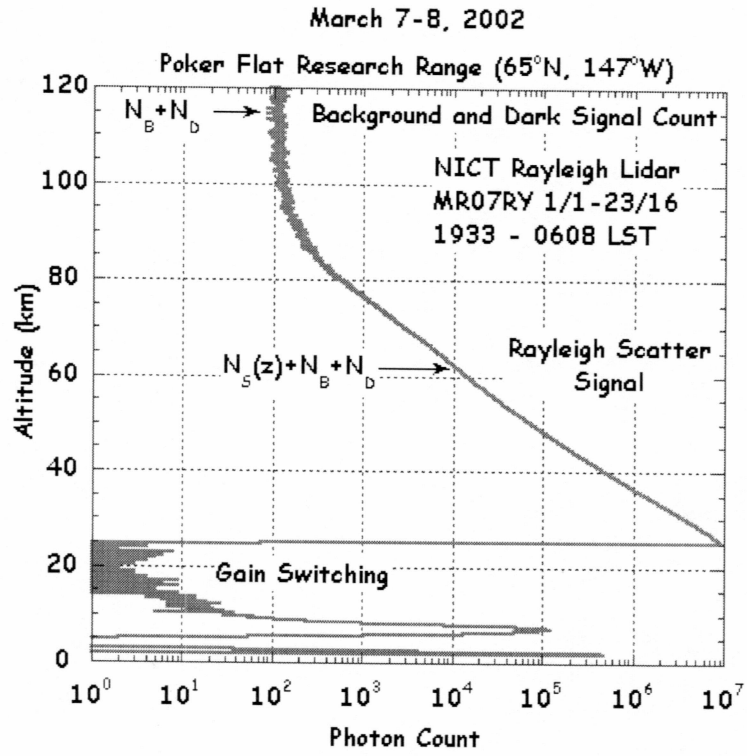

Figure 2.1: Photon count profile plotted as a function of altitude. This profile was measured by the NICT-Rayleigh lidar at PFRR on the night of March 7-8, 2002. The profiles were acquired by integrating the echoes from 736,000 laser shots over 10 h 35 min.

The signal in Figure 2.1 is not smooth and fluctuations are evident. These fluctuations arise due to the statistical nature of the photon counting process, where the photon count signal is a Poisson random variable [Papoulis, 1984]. For an expected photon count signal of value N, there is an inherent variance of $\sqrt{N}$. Thus, the relative error in any photon count signal is given by,

$$\frac{\Delta N}{N} = \frac{\sqrt{N}}{N} = \frac{1}{\sqrt{N}} \qquad (2.4)$$

Thus the uncertainty in the signal $N_s(z)$ given by,

$$\frac{\Delta N_S}{N_S} = \frac{\Delta N}{N_S} = \frac{\sqrt{N}}{N_S} = \frac{\sqrt{N_S + N_D + N_B}}{N_S} \qquad (2.5)$$

The relative uncertainties in the photon count profile in Figure 2.1 are calculated for five altitudes in Table 2.1. We see that the relative error increases from 0.1% at 40-45 km to 88% at 120-125 km.

Ideally, using a perfect detector under a dark sky, dark counts and background counts would be zero, i.e., the detector is not noisy, and there is no skylight. Then the relative uncertainty in the photon count signal decreases to $1/\sqrt{N_S}$. Δt is the temporal resolution of the raw photon count signal. Δz is the spatial resolution of the raw photon count profile. By integrating the photon count profiles in either space or time or both, the product of the resolution parameters $\Delta t \times \Delta z$ is increased by some factor k, and the signal photon count increases (i.e., $N_S \rightarrow kN_S$). The background and dark counts are also increased by the same factor (i.e., $N_D \rightarrow kN_D$, $N_B \rightarrow kN_B$). Thus, the relative error becomes,

$$\frac{\Delta N_S}{N_S} \rightarrow \frac{\sqrt{kN_S + kN_B + kN_D}}{kN_S} = \frac{\sqrt{N_S + N_B + N_D}}{\sqrt{k}N_S} = \frac{\Delta N_S}{\sqrt{k}N_S} \qquad (2.6)$$

and the statistical quality of the photon data improves by a factor $\sqrt{k}$. Thus the raw photon count profile can be acquired at high-resolution (e.g., Δz = 75 m, Δt = 50 s) and subsequently analyzed at lower resolution (e.g., Δz = 2 km, Δt = 15 min) with an associated improvement in statistical quality (e.g., $\sqrt{k}$ = 22). If the instrumental parameters of K_{sys}, were increased (e.g., laser energy increased, repetition rate of laser increased, telescope area increased) then the photon count signal $N_S(z)$ would again increase and improve the statistical quality of the lidar measurements.

Table 2.1: Photon count statistics for March 7-8, 2002

Altitude (km)[1]	Photon Counts N	Signal Count[2] N_s	Relative error $\Delta N_s/N_s$ (%)
42.5	308466	308366	0.18
62.5	10059	9960	1.0
82.5	402	302	6.6
102.5	121	21	52
122.5	112	12	88

1. Altitude at the center of range. For 42.5 km with an altitude resolution of 5 km the photon count signal integrated over 40 to 45 km altitude range.
2. The estimate of the background and dark counts is taken as the average of the photon counts in the 220-225 km altitude range.

The photon count profiles are then used to calculate the density profiles using the lidar equation (Eqns. 2.1 and 2.2) and standard inversion methods [Wang, 2003]. The density profile is normalized to one at the lowest altitude (e.g., 40 km) yielding a relative density profile. This keeps the measurement of the relative density independent of the other parameters. The relative density profile estimated from the total photon count profile in Figure 2.1 is plotted in the upper panel of Figure 2.2. The density profile

decays exponentially with altitude with a scale height, H, of 7.4 km ($H = R_{air}T/g$, where R_{air} is the gas constant for air (= 287 J/(kg-mol)), g = 9.5 m/s^2 and T is the average temperature).

$$\frac{N_S(z_2)}{N_S(z_1)} = \frac{\dfrac{\rho(z_2)}{z_2^2}}{\dfrac{\rho(z_1)}{z_1^2}} \tag{2.7}$$

Thus we can derive a relative density profile $r(z, z_0)$ from the raw lidar signal,

$$r(z, z_0) = \frac{\rho(z)}{\rho(z_0)} \tag{2.8}$$

$$= \frac{N_S(z)}{N_S(z_0)} \times \frac{z^2}{z_0^2} \tag{2.9}$$

$$= \frac{N(z) - N_B}{N(z_0) - N_B} \times \frac{z^2}{z_0^2} \tag{2.10}$$

The temperature profile from the corresponding photon count profile is computed using the relative density profile and the hydrostatic retrieval method [e.g., Cutler, 2000; Wang, 2003].

$$T(z) = T(z_0) \times \frac{\rho_n(z_0)}{\rho_n(z)} + \frac{M_{air}}{R} \int_z^{z_0} \frac{\rho_n(x)}{\rho_n(z_2)} \times g(x) \times dx \tag{2.11}$$

$$T(z) = T(z_0) \times r(z_0, z) + \frac{M_{air}}{R} \int_z^{z_0} r(x, z) \times g(x) \times dx \tag{2.12}$$

where M_{air} is the Molecular mass of the dry air (0.029 kg/mol) and R is the universal gas constant (8.31 J/mol-K). The temperature profile corresponding to the relative density profile is plotted in the lower panel of Figure 2.2. In calculating the temperature profile from the density profile, the MSISE-90 model from NASA was used to provide an initial

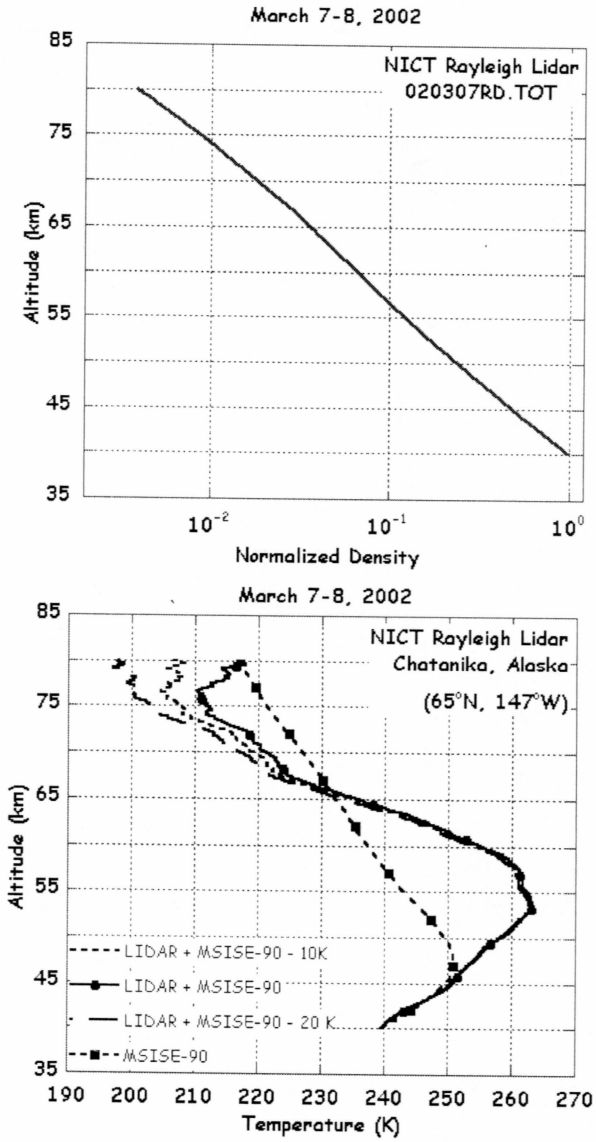

Figure 2.2: Temperature and density profiles plotted as a function of altitude. (Upper) Density profile retrieved from the photon count profile, normalized to one at 40 km. (Lower) Temperature profile (solid) computed from the density profile and MSISE-90 model at 80 km (dash dot), MSISE-90 model minus 10 K (short dash), MSISE-90 model minus 20 K (long dash),

temperature estimate at 80 km. We observe that the temperature measured by the Rayleigh lidar is warmer in the stratosphere than the MSISE-90 temperature. The maximum temperature of 263.5 K occurs at the stratopause altitude of 53.5 km. A local minimum of 210.5K occurs at about 76 km. In Figure 2.2 we also plot the temperature profiles using the MSISE-90 temperature at 80 km minus 10 K (short dash) and minus 20 K (long dash). We see that the temperature profile converges at about 65 km. This minimum is an artifact of seed initialization at 80 km. It has also been observed that the mesosphere is actually colder by about 10 K than MSISE-90 [Collins et al., 2003]. The average measured temperature over the 40-80 km altitude range is 240.4 K consistent with the density scale height of 7.4 km.

Section 2.2: Gravity Waves

The relative temperature perturbations at scales of several km in the middle atmosphere have been understood since the 1960's, and arise due to the presence of buoyancy, or gravity, waves in the atmosphere [Hines, 1960]. Gravity waves are small-scale (i.e., horizontal wavelengths of ~100-1000 km, vertical scales of ~ 1-10 km, periods of ~ 300 s – ~10 h) waves that result from the balance of inertia and buoyancy forces. The perturbations at these scales maybe expressed in two dimensions (time, t, and altitude, z,) as the summation of an ensemble of n waves,

$$r_T(t,z) \triangleq \sum_{i=1}^{n} R_{T_i}(z)\cos(\omega_i t_t - m z_i + \phi_i) \qquad (2.13)$$

where each individual wave has amplitude R_{T_i}, frequency ω_i, vertical wave number m_i, and phase ϕ_i. The wave amplitude, R_{T_i}, grows with altitude as the wave energy is constant with altitude. As the density of atmosphere decreases with altitude ($\sim e^{-z/H}$, where H ~ 7.4 km), the amplitude of the fluctuations grows to maintain constant wave energy with altitude (i.e., $R_{T_i}(z) \sim e^{z/2H}$) and eventually the waves become unstable and break. The physics of these processes and the contribution to the general circulation

remains an area of active research (see discussion by Fritts and Alexander [2003]). The rms temperature fluctuation at a given altitude given by,

$$r_{T\,rms}(z) = \frac{1}{2n}\sqrt{\sum_{i=1}^{n} R_{T_i}(z)^2} \qquad (2.14)$$

is a measure of the wave power and is used to quantify the wave activity. The rate at which the rms amplitude varies with altitude gives a measure of how the gravity waves are propagating with altitude and whether they are loosing power as they propagate. For example, Collins and Smith [2004] considered the exponential growth of gravity waves with altitude in the mesopause region (~ 80-100 km),

$$r_{T\,rms}(z) \sim \exp(-z/H_g) \qquad (2.15)$$

and compared the observed scale height, Hg, with the scale for freely-propagating waves, 2H. Collins and Smith found that $H_g < 2H$ and concluded that the waves are losing energy with altitude due to nonlinear interactions between different waves in the ensemble.

In this study our goal is to develop methods for accurately determining the gravity wave activity from Rayleigh lidar temperature measurements.

Section 2.3: Calculation of Relative Temperature Perturbations

Integrating the photon counts over the complete night gives a statistically robust signal for computation of the temperature profile, but prevents us from examining gravity-wave variations in temperature during the night. The temperature profile computed from the total photon count profile may not represent the actual long-term temperature, as long-period waves and tides that are longer than the observation period may be present. To understand the variations during the night, we compute the fluctuations or perturbations over the night. Perturbations are changes in the value of a

quantity (e.g., temperature, density, wind or concentration) relative to a constant background or ambient atmospheric value.

As a case study, we use the measurements from the night of March 7-8, 2002. This night is chosen due to the high quality of the data. We divide the observation period into 11 one-hour (or 60-min) intervals, yielding 11 integrated photon count profiles. We follow the methodology of Wang [2003] and calculate the combined background and dark photon count signal at 225 km and correct the photon count profiles for extinction. We then smooth the photon count profiles with a 2-km running geometric average (i.e., exponential smoothing). We then calculate the sequence of 11 temperature profiles. We do not apply any further spatial filtering to the temperature profiles in this chapter. The 60-min profiles are plotted in the upper panel of Figure 2.3. The conventional and simplest approach to estimate the background profile is to compute the average (or mean) temperature profile, $T_{AVG}(z)$, over the complete observation period, T_{obs},

$$T_{AVG}(z) = \frac{1}{T_{obs}} \int_0^{T_{obs}} T(t,z)dt \tag{2.16}$$

or in terms of the discretely sampled data

$$T_{AVG}(j) = \frac{1}{n1} \times \sum_{i=1}^{n1} T(i,j) \tag{2.17}$$

where n1 (= 11) is the number of the profiles that are made during the observation period, i is the time index (i = 1,... 11) corresponding to times 2000, 2100, ... 0600 LST, n2 (=534) is the number of samples in altitude and j is the altitude index (j = 1,... n2, (= 534)) corresponding to altitudes 40.050, 40.130, ... 80.030. The average of the 11 profiles is also plotted in the upper panel of Figure 2.3. The average temperature profile is plotted with the sample standard deviation in the lower panel of Figure 2.3. In Figure 2.3, all of the 60-min profiles converge to the average profile at 80 km. This is because the temperature at 80 km is taken as constant from the MSISE-90 profile for the complete

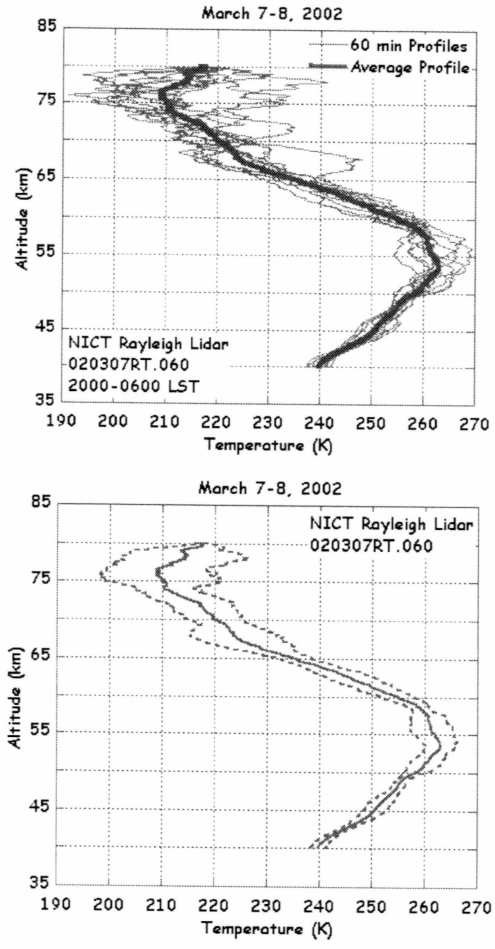

Figure 2.3: NICT Rayleigh lidar temperature profiles plotted against altitude. (Upper panel) Sixty-min temperature profiles (thin) and average (thick). Each 60-min temperature profile is computed from a photon count profile integrated for 60 min of photon count signal. (Lower panel) The average of the 60-min profiles (solid) with errors (dashed).

night. This produces certain artifacts in the structure of the temperature profile because the errors at the higher altitudes (70-80 km) are largest, and restricting the value to a constant allows more spectral components to be seen than are actually present. The errors at higher altitudes are larger than those at any other altitude ranges. The uncertainty due to photon count statistics in the individual 60-min profiles is approximately 1.25 K at the stratopause altitude of 53.5 km. The sample standard deviation of the average profile at the stratopause is 2.84 K indicating an uncertainty in the average value of 0.86 K. In comparison the uncertainty due to photon count statistics in the total temperature profile (Figure 2.2) is approximately 0.38 K at the stratopause. At 40 km the uncertainty due to photon count statistics in the individual 60-min profiles is approximately 0.25 K, the uncertainty in the sample mean is 0.45 K, and the uncertainty due to photon count statistics in the total temperature profile (Figure 2.2) is 0.075 K.

We define relative temperature perturbation, $r_T(t,z)$, as the ratio of the difference between the perturbed temperature $T(t,z)$ and the unperturbed (or background or ambient) temperature $T_{BKG}(z)$ to the background temperature:

$$r_T(t,z) \triangleq \frac{T(t,z) - T_{BKG}(z)}{T_{BKG}(z)} \tag{2.18}$$

The relative temperature perturbations in the atmosphere arise due to the presence of buoyancy, or gravity, waves in the atmosphere [Hines, 1960]. The perturbations maybe expressed in two dimensions (time, t, and altitude, z,) as the summation of an ensemble of n waves,

$$r_T(t,z) \triangleq \sum_{i=1}^{n} R_{T_i}(z)\cos(\omega_i t - m_i z + \phi_i) \tag{2.19}$$

where each individual wave has amplitude R_{T_i}, frequency ω_i, vertical wave number m_i, and phase ϕ_i. We use the 11 profiles and average profile in Figure 2.3 to calculate the sequence of 11 relative temperature profiles,

$$r_T(i,j) \triangleq \frac{T(i,j) - T_{BKG}(j)}{T_{BKG}(j)} \qquad (2.20)$$

We plot the sequence of relative temperature profiles in Figure 2.4. The profiles in Figure 2.4 show several distinct features; the amplitude of the perturbations appears to grow with altitude and downward propagating features are present in successive profiles (e.g., at 45 km at 2200 LST, 57 km at 0230 LST and 70 km at 0230 LST.). These characteristics are typical of gravity waves. Gravity waves grow in amplitude with altitude as they maintain their energy as the atmosphere becomes less dense with altitude. Gravity waves exhibit downward phase progressions as they propagate upward [Hines, 1960].

We characterize the gravity-wave activity in terms of the mean square (ms) and root mean square (rms) amplitude of the relative temperature perturbations. The ms amplitude gives the measure of the power of wave-induced perturbations [Wang, 2003]. We compute the mean of the perturbations in both time and altitude,

$$\overline{r_t}(i) = \frac{\sum_{j=1}^{n1} r(i,j)}{n1} \qquad (2.21)$$

$$\overline{r_z}(j) = \frac{\sum_{i=1}^{n2} r(i,j)}{n2} \qquad (2.22)$$

before computing the ms and rms amplitudes of these space-time perturbations. These averages are subtracted from the relative temperature perturbations to yield true zero-mean fluctuations,

$$r'(i,j) = r(i,j) - \overline{r_z}(j) - \overline{r_t}(i) \qquad (2.23)$$

The perturbation power is the mean square of these perturbations

$$P_r = \frac{\sum_{j=1}^{n1}\sum_{i=1}^{n2} r'(i,j)^2}{n1 \times n2} \qquad (2.24)$$

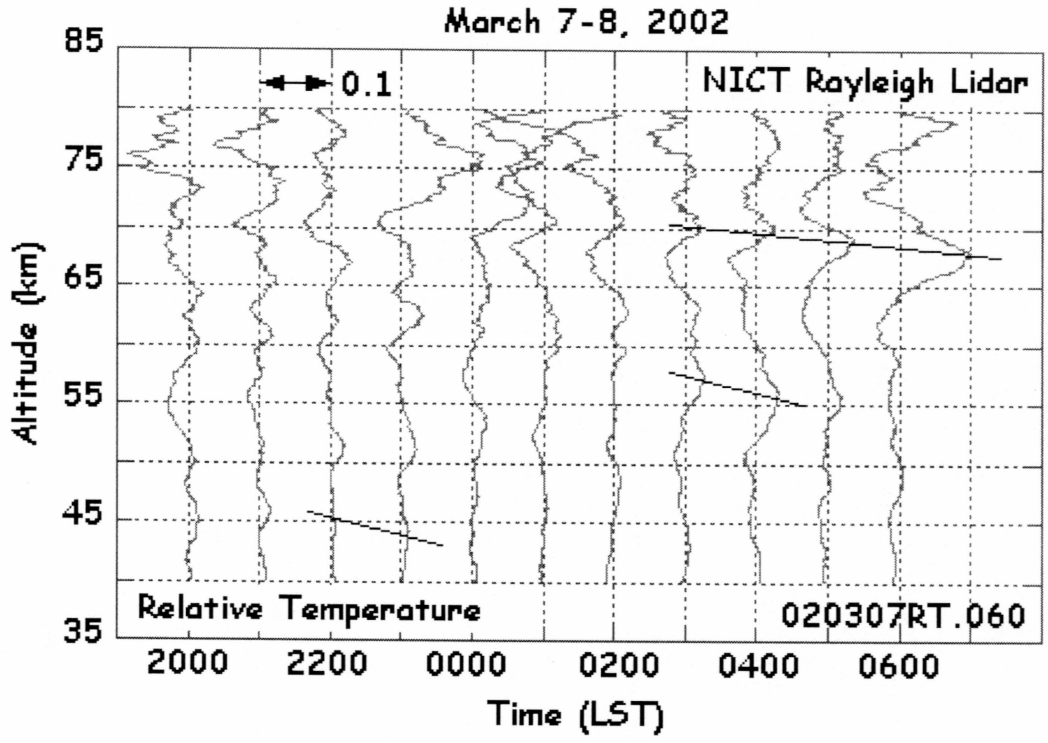

Figure 2.4: Sequence of relative temperature profiles plotted as a function of altitude. The profiles are calculated from 60-min temperature profiles. The successive profiles are offset by 0.1. Downward phase progressions are identified at 45 km at 2200 LST, 57 km at 0300 LST and 70 km at 0300 LST. The phase progressions are characteristic of upwardly propagating gravity waves.

The rms amplitude is then computed as a percentage perturbation,

$$r_{rms} = \sqrt{P_r} \times 100 \tag{2.25}$$

The rms amplitudes for various altitude ranges are tabulated in Table 2.2. The rms amplitude of the perturbations increases with increasing altitude. The rms perturbation over the entire 40 km (2.18%) is greater than the ms average of the 10 km intervals (1.77%) because the average over 40 km includes wave components with periods between 30 and 10 km.

Table 2.2: Altitude variations of rms relative temperature perturbations

Altitude Range	40-50 km	50-60 km	60-70 km	70-80 km	40-80 km
RMS Amplitude (%)	0.50	1.01	2.06	2.64	2.18

Average background profile is used.

Section 2.4: Determination of Background Temperature

If the average profile represents the background profile for the observation period, it would underestimate the contribution to the wave field made by the motions with periods greater than the observation period [Mitchell et al., 1990]. We consider four standard methods for estimating the background temperature profile from the average temperature profile:

i. The average temperature profile is low-pass filtered with a brick-wall filter of 6-km cutoff

ii. A third-order polynomial fit is made to the average temperature profile

iii. A running average of length 6 km is applied to the average temperature profile

iv. A spline fit, at a resolution of 6 km, is made to the average temperature profile after a running average of 6 km has been applied to the average temperature profile.

We calculate the rms temperature perturbations using each of these background profiles to determine if there are systematic differences or biases in the estimates of gravity-wave activity based on choice of background profile.

i. Low-Pass Filtering

The spatial average of the average temperature profile, T_{avgZ},

$$T_{avgZ} = \frac{1}{n1} \sum_{j=1}^{n1} T_{AVG}(j) \tag{2.26}$$

is first subtracted from the average temperature profile, T_{avg},

$$T_1 = T_{AVG} - T_{avgZ} \tag{2.27}$$

This procedure prevents oscillations in the filtered data due to the Gibbs phenomenon [e.g., Oppenheim et al., 1983]. We then low-pass filter the profile, T_1, with a filter cutoff of 6 km to yield a profile T_2,

$$T_2 = \mathcal{L}(T_1) \tag{2.28}$$

Finally, we add T_{avgZ} back to the filtered profile to obtain the low-pass filtered profile, T_{LPF},

$$T_{LPF} = T_2 + T_{avgZ} \tag{2.29}$$

We plot the low-pass filtered temperature profile, T_{LPF}, in the upper left panel of Figure 2.5.

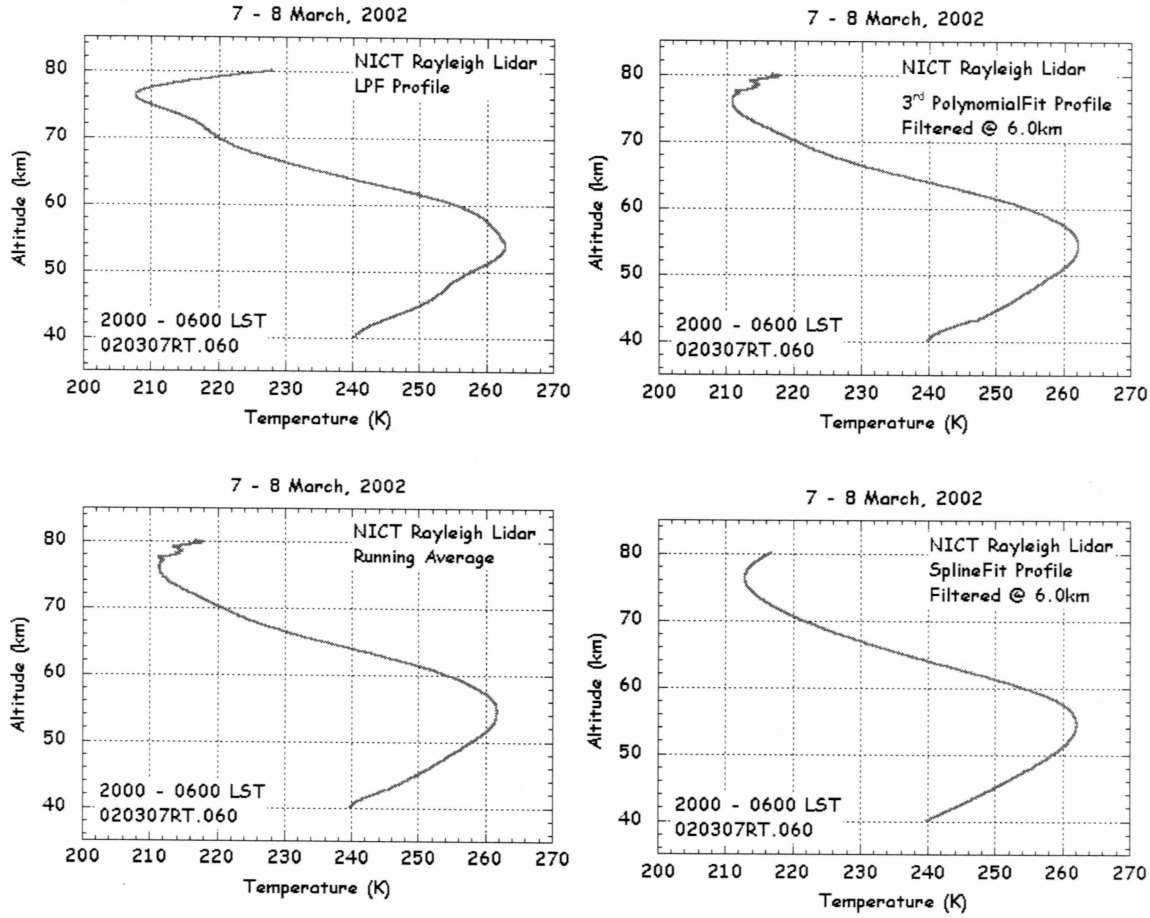

Figure 2.5: Background temperature profile plotted with altitude. The background profile is calculated using four different methods. (Upper left) Low pass filtering of the average temperature profile. (Upper Right) Third-order polynomial fit of the average temperature profile. (Lower Left) Running average of the average temperature profile. (Lower Right) Spline fit to the average temperature profile. (See text for details).

ii. Polynomial Fit

We perform a weighted least-square third-order polynomial fit to the average temperature T_{AVG}, to yield a profile, T_1,

$$T_1 = \mathcal{P}(T_{AVG}) \tag{2.30}$$

We then determine the low-wavenumber component of the difference between the polynomial fit and the average profile by applying a 6-km running average (i.e., smoothing) to the difference profile, T_2, to yield T_3,

$$T_2 = T_{AVG} - T_1 \tag{2.31}$$

$$T_3 = \mathcal{R}(T_2) = \frac{1}{w} \times \sum_{k=j-w/2}^{(j+w/2)} T_2(k) \tag{2.32}$$

where w (= 81) is the length of the window of running average. We then add the smoothed difference profile, T_3, to the third-order polynomial fit profile, T_1, to yield the polynomial fit temperature profile, $T_{Polyfit}$,

$$T_{Polyfit} = T_1 + T_3 \tag{2.33}$$

We plot the polynomial temperature profile, $T_{Polyfit}$, in the upper right panel of Figure 2.5.

iii. Running Average

We smooth the average temperature profile, T_{AVG}, with a running average window of 6 km width, to yield a running average temperature profile, T_{RA},

$$T_{RA} = \mathcal{R}(T_{AVG}) \tag{2.34}$$

We plot the running average temperature profile, T_{RA}, in lower left panel of Figure 2.5.

iv. Spline Fit

We smooth the average temperature profile using a running average over 6 km and then apply a third-order spline fit [Press et al., 1992] to the smoothed average to yield, T_{spline},:

$$T_{spline} = \mathcal{S}(\mathcal{R}(T_{AVG})) \quad (2.35).$$

The spline fit temperature profile, T_{spline}, is plotted in the lower right panel of Figure 2.5.

We plot the differences between the four background profiles and the average temperature profile in Figure 2.6. Several features in Figure 2.5 and Figure 2.6. are worth noting. In the upper left panel, T_{LPF}, exhibits overshoot due to Gibbs phenomenon at 80 km. In the upper right and lower left panels, $T_{Polyfit}$ and T_{RA} show no difference relative to the average profile in the first and last 3 km. This is because the running average window leaves the first and last half window unsmoothed. In the lower right panel, T_{spline} has the largest difference with the average temperature profile above 65 km. All of the difference profiles in Figure 2.6 show an approximately 6-km ripple or oscillation due to the spatial smoothing and/or filtering of the average temperature profile at 6 km inherent in all four methods.

We computed the rms amplitude of the temperature perturbations over intervals of 10 km in the 40-80 km altitude range. We present the results in Table 2.3. We note that there is no significant difference in the rms amplitude estimates due to different choice of background profile. In the 40-50 km range, all methods (as well as the average temperature profile (Table 2.2)) yield an rms relative temperature amplitude of 0.5%. In the 50-60 km range, all methods yield an rms relative temperature amplitude of 1.01%. In the 60-70 km range, all methods yield an rms relative temperature amplitude of 2.06%, except for the spline fit estimate of 2.05%. At the highest altitude range of 70-80 km, the different methods yield a range of values from 2.62% to 2.65%. Over the whole altitude range of 40-80 km, the methods yield a range of values from 2.16% to 2.18%. We also

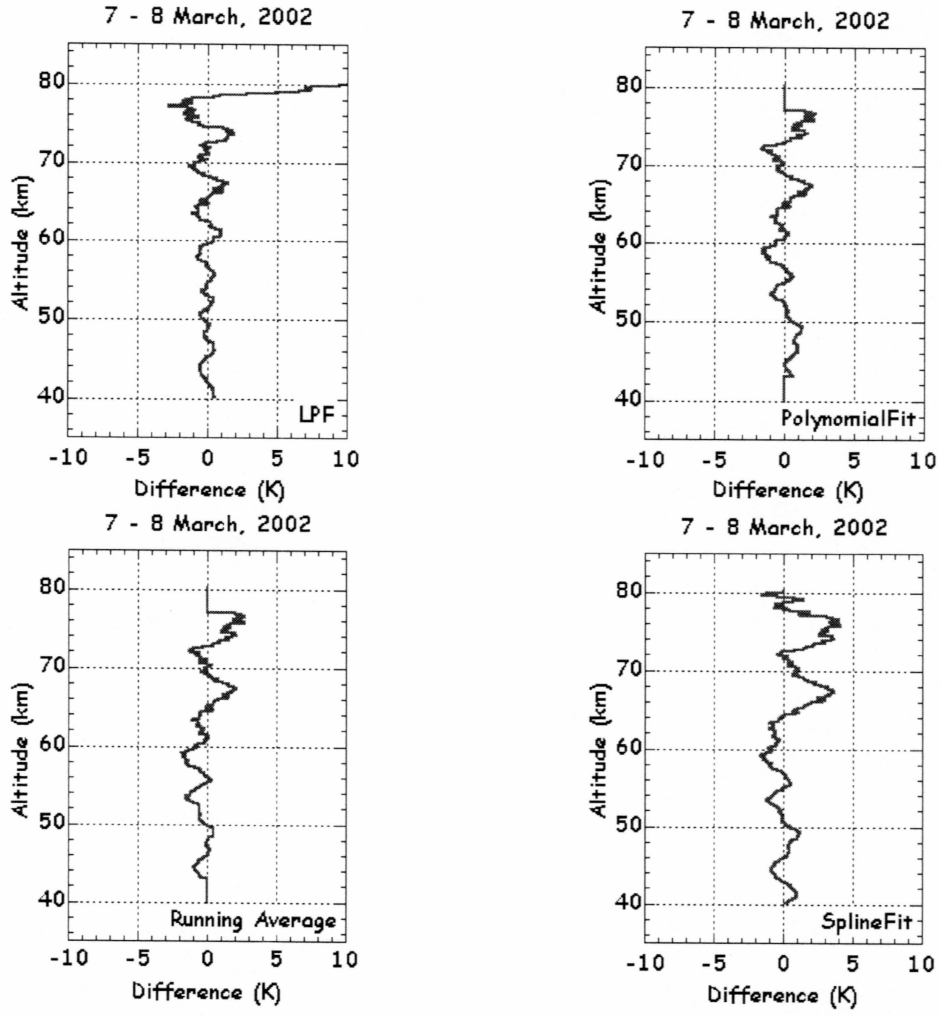

Figure 2.6: Difference between various background temperature profiles and the average temperature profile plotted with altitude. (Upper left) Difference with low pass filtering of the average temperature profile. (Upper Right) Difference with third-order polynomial fit of the average temperature profile. (Lower Left) Difference with running average of the average temperature profile. (Lower Right) Difference with spline fit to the average temperature profile. (See text for details).

note again that the rms amplitude of the relative temperature perturbations grows with altitude in all cases.

Table 2.3: Altitude variations of rms temperature perturbation profiles for four backgrounds

Altitude Range	RMS Amplitude (%)			
	Low Pass Filter	Polynomial Fit	Running Average	Spline Fit
40-50 km	0.50	0.50	0.50	0.50
50-60 km	1.01	1.01	1.01	1.01
60-70 km	2.06	2.06	2.06	2.05
70-80 km	2.65	2.64	2.63	2.62
40-80 km	2.18	2.17	2.17	2.16

Section 2.5: Conclusion

We conclude from Table 2.2 and Table 2.3 that the estimate of the rms amplitude of the relative temperature perturbations does not vary significantly with the choice of the background profile. Therefore, we conclude that the choice of background profile does not affect the results in analyzing the relative temperature perturbations. In the further analysis of the perturbations, we will use the average temperature profile as the background temperature profile.

Chapter 3. Estimation of Noise Power Contribution to Relative Temperature Perturbation Power

Section 3.1: Introduction

In Chapter 2, we calculated the total power in the temperature perturbations without consideration of the relative contribution of the gravity wave perturbations (i.e., the signal) and the photon count uncertainties inherent in the lidar measurement (i.e., the noise). The perturbation power in Chapter 2 is an overestimate of the actual temperature perturbation power due to atmospheric gravity waves. In this chapter we use spectral analysis techniques to calculate the noise component of the total perturbation power. We then subtract this noise power from the total perturbation power to yield the signal perturbation power and determine the signal-to-noise ratio (SNR) of the measurements. We examine the variations in the rms perturbation due to time resolution of the data, smoothing of photon counts and band limiting in space and time. As in Chapter 2, we illustrate our approach with the measurements from the March 7-8, 2002 observations.

Section 3.2: Perturbation Spectrum

The power spectrum of a signal in the time (or space) domain is the distribution of power in frequency (or wavenumber) [e.g., Oppenheim et al., 1983]. The wavenumber spectrum of each relative temperature perturbation profile, $r_T(i, j)$ $(j = 1, n2)$ is calculated using the periodogram method [Koopmans, 1974]. The periodogram estimates the spectrum as the square of the magnitude of the Fast Fourier Transform (FFT),

$$F_T(i,k) = \mathcal{FFT}(r'_T(i, j)) \tag{3.1}$$

$$S_T(i,k) = \left|F_T(i,k)\right|^2 \times k_{norm} \tag{3.2}$$

where $k_{norm} = nfft \times \Delta t \times nfft/n2$. We zero-pad the original *n2* point altitude profiles to yield an *nfft* (e.g., 1024) length sequence. The value of *nfft* is chosen to be a power of 2 just larger than the original length *n2*,

$$nfft = 2^n \geq n2 \tag{3.3}$$

The spectra are normalized by k_{norm} so that the integral of the spectrum yields the average power in the perturbations in accordance with Parseval's Theorem,

$$\sum_{i=1}^{nfft} S_T(i,k) \cdot \Delta m = \frac{1}{n2} \sum_{j=1}^{n2} r_T'(i,j)^2 \tag{3.4}$$

where $\Delta m = 1/(nfft \times \Delta z)$ ($=1.30 \times 10^{-2}$ km^{-1}).

We compute the average wavenumber spectrum of the relative temperature perturbation over the entire observation period, S_T, by averaging the spectra of the *n1* individual profiles.

$$S_T(k) = \frac{1}{n1} \sum_{i=1}^{n1} S_T(i,k) \tag{3.5}$$

The average wavenumber spectrum, $S_T(k)$, is plotted in Figure 3.1. This spectrum represents the average of eleven spectra of the individual perturbation profiles. The spectrum extends from –6.67 km^{-1} to 6.67 km^{-1}. The value 6.67 km^{-1} is the Nyquist wavenumber (= 1/(2× 0.075) km^{-1}) corresponding to the altitude sampling resolution of 0.075 km. We plot the positive half of the spectrum in Figure 3.1 as the negative half is identical, since the perturbation profiles are real numbers. The spectra is of relative temperature perturbation profiles that have not been low pass filtered and were derived from photon count profiles that have not been smoothed.

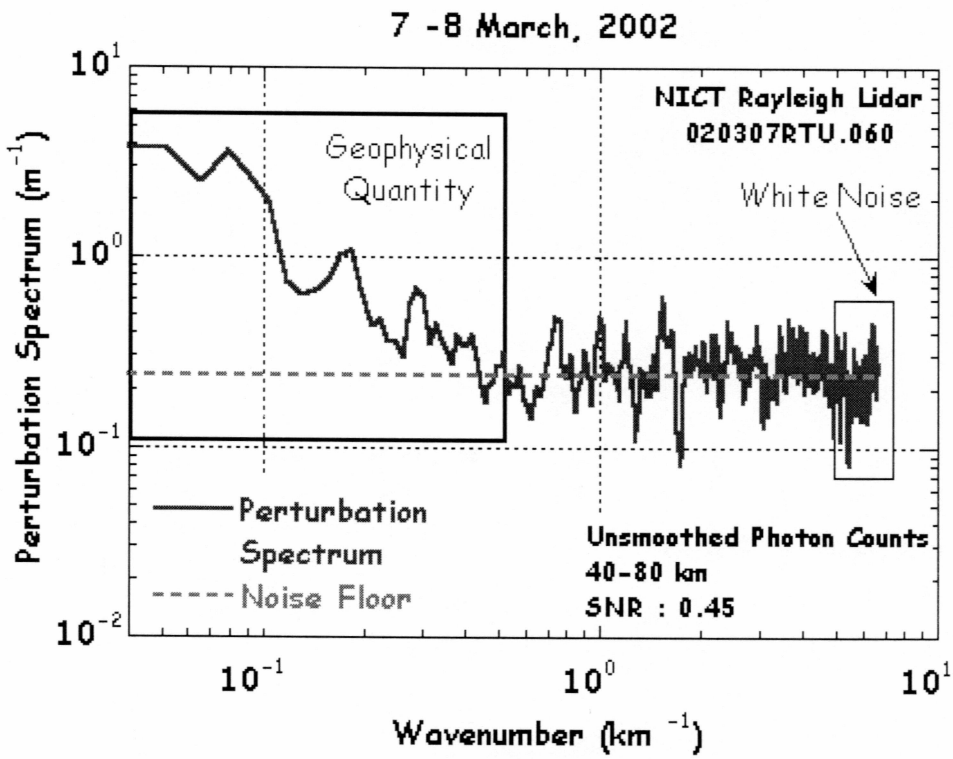

Figure 3.1: Average perturbation spectrum plotted as a function of wavenumber. This spectrum represents the average of 11 spectra of individual temperature perturbation profiles.

The perturbation at each altitude is the sum of a deterministic component due to gravity waves and a noise component due to the statistics of the counting process. Thus, we interpret the spectrum in Figure 3.1 as the superposition of a deterministic base-band spectrum (the signal component) and a statistical white noise spectrum (the noise component). We model the measurement noise as a classic additive white noise [e.g., Carlson, 1986].

Section 3.3: Determination of Noise Characteristics

We expect that if the noise portion of the periodogram spectrum is indeed white noise, then it should have certain characteristics,

i. The variance of the periodogram of white noise equals the expected spectral value of the periodogram

ii. The autocorrelation function of the white noise is a delta function.

We analyze both the spectra and autocorrelation function of the relative temperature perturbations to determine whether the signals have these characteristics.

To investigate the spectral properties, we calculate the sample mean and standard deviation of the spectrum in the high-wavenumber range (5.5 km^{-1} – 6.67 km^{-1}). We term this sample mean of the spectrum as the noise floor. We calculate the sample mean and standard deviation for each of the individual wavenumber spectra as well the average spectrum. We present the results in Table 3.1. We see that the ratio of the standard deviation to the mean is approximately one for the individual spectra. For the average spectrum the ratio is 0.308. The average spectrum is the average of 11 individual spectra and so the standard deviation is a factor $\sqrt{11}$ (= 3.32) smaller than that of the individual spectrum. The value of the ratio of the standard deviation to the mean of 0.308 implies a value of 1.02 for the individual profile spectrum, in agreement with the theoretical value of one for a white noise process [Koopmans, 1974].

To investigate the correlation properties, we calculate the autocorrelation function by taking the Inverse Fourier Transform of the average wavenumber spectrum [e.g., Oppenheim et al,.1983]. We calculate the autocorrelation function from both the entire spectrum (Figure 3.2 upper) and from the high-wavenumber (5.5 km^{-1} – 6.67 km^{-1}) portion of the spectrum (Figure 3.2 lower). We see that the autocorrelation function has a narrow spike at zero-lag. The autocorrelation function of the full spectrum has the narrow spike superimposed on a broader function. The autocorrelation function of the high-wavenumber portion of the spectrum has a narrow spike and much smaller fluctuating values at non-zero lags. The amplitude of the spike is one while the average value of the non-zero lags is 0.006 and the standard deviation of the non-zero lags is 0.003. We conclude that the correlation functions are consistent with the model of a base-band or low-wavenumber signal (broad autocorrelation function) and an additive white noise (narrow delta-function autocorrelation function) [Oppenheim et al., 1983].

Table 3.1: Mean and standard deviation of spectral noise floor

Time (LST)	Noise floor (μ)	Standard Deviation (σ)	σ/μ
2000	0.527	0.374	0.709
2100	0.281	0.216	0.767
2200	0.340	0.302	0.889
2300	0.171	0.129	0.754
0000	0.251	0.218	0.867
0100	0.176	0.181	1.030
0200	0.219	0.197	0.899
0300	0.145	0.174	1.190
0400	0.134	0.114	0.854
0500	0.188	0.171	0.910
0600	0.199	0.312	1.560
Average Profile	0.239	0.074	0.308

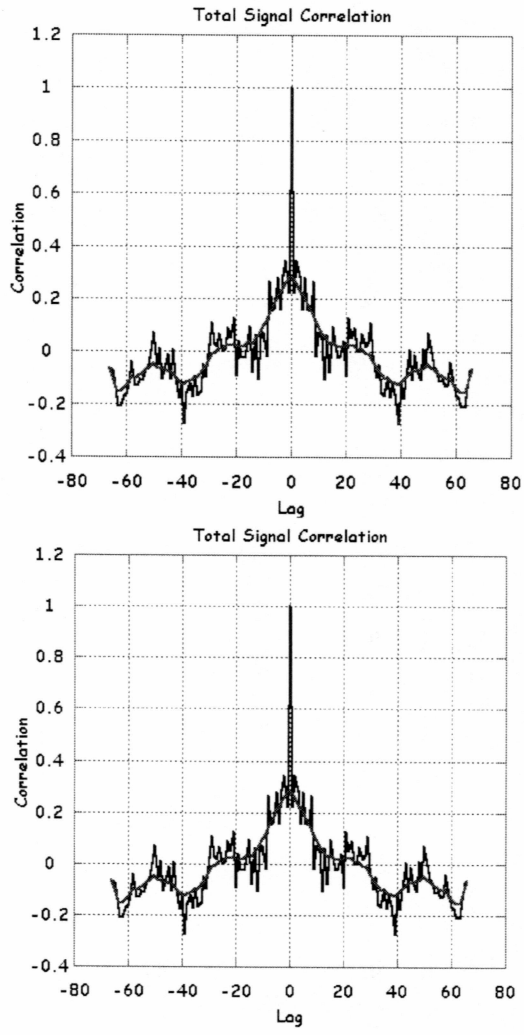

Figure 3.2: Autocorrelation function of relative temperature perturbations plotted as a function of spatial lag. The autocorrelation function is calculated by taking the Inverse Fourier Transform of the average wavenumber spectrum. (Upper) Autocorrelation function derived from entire spectrum. A 5-point running average is superimposed on the autocorrelation function (thick). (Lower) Autocorrelation function derived from high-wavenumber (5.5 km^{-1} – 6.67 km^{-1}) portion of spectrum.

Section 3.4: Estimation of Signal, Noise and Signal to Noise Ratio

We characterize the amplitude of the noise spectrum by the average value of the relative temperature spectrum over the high wavenumber range 5.5-6.67 km^{-1}. We call this average the noise floor, N_{FLR}, given by

$$N_{FLR} = \frac{1}{nz} \times \sum_{k=nz1}^{nz2} S_T(k) \tag{3.6}$$

where nz_1 corresponds to wavenumber 5.5 km^{-1}, nz_2 corresponds to the wavenumber 6.67 km^{-1} and nz = nz2-nz1+1. We calculate the total noise power of all wavenumbers, N, as,

$$N = N_{FLR} \times nfft \times \Delta m \tag{3.7}$$

We calculate the total power in the spectrum P as

$$P = \sum_{k=1}^{nfft} S_T(k) \times \Delta m \tag{3.8}$$

We calculate the signal power in the spectrum S as,

$$S = P - N \tag{3.9}$$

We calculate the signal-to-noise ratio of over the total bandwidth of the signal, SNRT, as,

$$SNRT = \frac{P-N}{N} = \frac{\sum_{k=1}^{nfft} S_T(k) - N_{FLR} \times nfft}{N_{FLR} \times nfft} \tag{3.10}$$

For the spectrum in Figure 3.1 we calculate a total power, P, of 4.6×10^{-3} and a noise power, N, of 3.1×10^{-3}. Thus the signal power, S , is 1.5×10^{-3} and the signal to noise ratio, SNRT, is 0.45. Clearly, the low signal-to-noise-ratio reflects that the signal is band-limited to wavenumbers below 0.5 km^{-1}, while the noise fills the whole bandwidth up to 6.67 km^{-1}. We can improve the SNR by spatially low-pass filtering the data. Filtering the data at a cutoff wavenumber, m_c, eliminates all spectral components (and the associated power) at wavenumbers greater than m_c. We calculate the band-limited noise power at wavenumbers 0 to 0.5 km^{-1}, N_c, as,

$$N_c = N_{FLR} \times nc \times \Delta m \tag{3.11}$$

where there are nc spectral components with wavenumber less than or equal to m_c. We calculate the band-limited power in the spectrum, P_c, as

$$P_c = \sum_k S_T(k) \times \Delta m \qquad (3.12)$$

where we sum the spectral components that correspond to wavenumbers less than or equal to m_c. We calculate the signal power in the band-limited spectrum, S_c, as,

$$S_c = P_c - N_c \qquad (3.13)$$

We calculate the signal-to-noise ratio of the band-limited signal, SNRC, as,

$$SNRC = \frac{P_c - N_c}{N_c} = \frac{\sum_k S_T(k) - N_{FLR} \times nc}{N_{FLR} \times nc} \qquad (3.14)$$

For the spectrum in Figure 3.1, we calculate a band-limited power, P_c, of 1.4×10^{-3} and a band-limited noise power, N_c, of 2.4×10^{-4}. Thus the band-limited signal power, S_c, is 1.2×10^{-3} and the signal-to-noise ratio, SNRC, is 4.8.

We now calculate the relative temperature perturbation spectra for the altitude ranges 40-50 km, 50-60 km, 60-70 km and 70-80 km. We plot the average spectra for each of the altitude ranges in Figure 3.3. Each of the spectra have the same general characteristics as the average spectrum over the 40-80 km altitude region. They have a base-band component in the low-wavenumber region ($m < 0.5$ km^{-1}) and white noise component in the high-wavenumber region ($m > 5.5$ km^{-1}). We see in Figure 3.4 that the amplitude of the noise floor increases with the increasing altitude range. For each of the spectra we calculate the noise floor, SNRT and SNRC, and tabulate the results in Table 3.2. From Table 3.2 we see that the noise floor increases by 8 dB with each increase in 10 km altitude range. SNRC is a factor of 10 greater than SNRT for altitudes up to 70 km. SNRC decreases with increase in altitude.

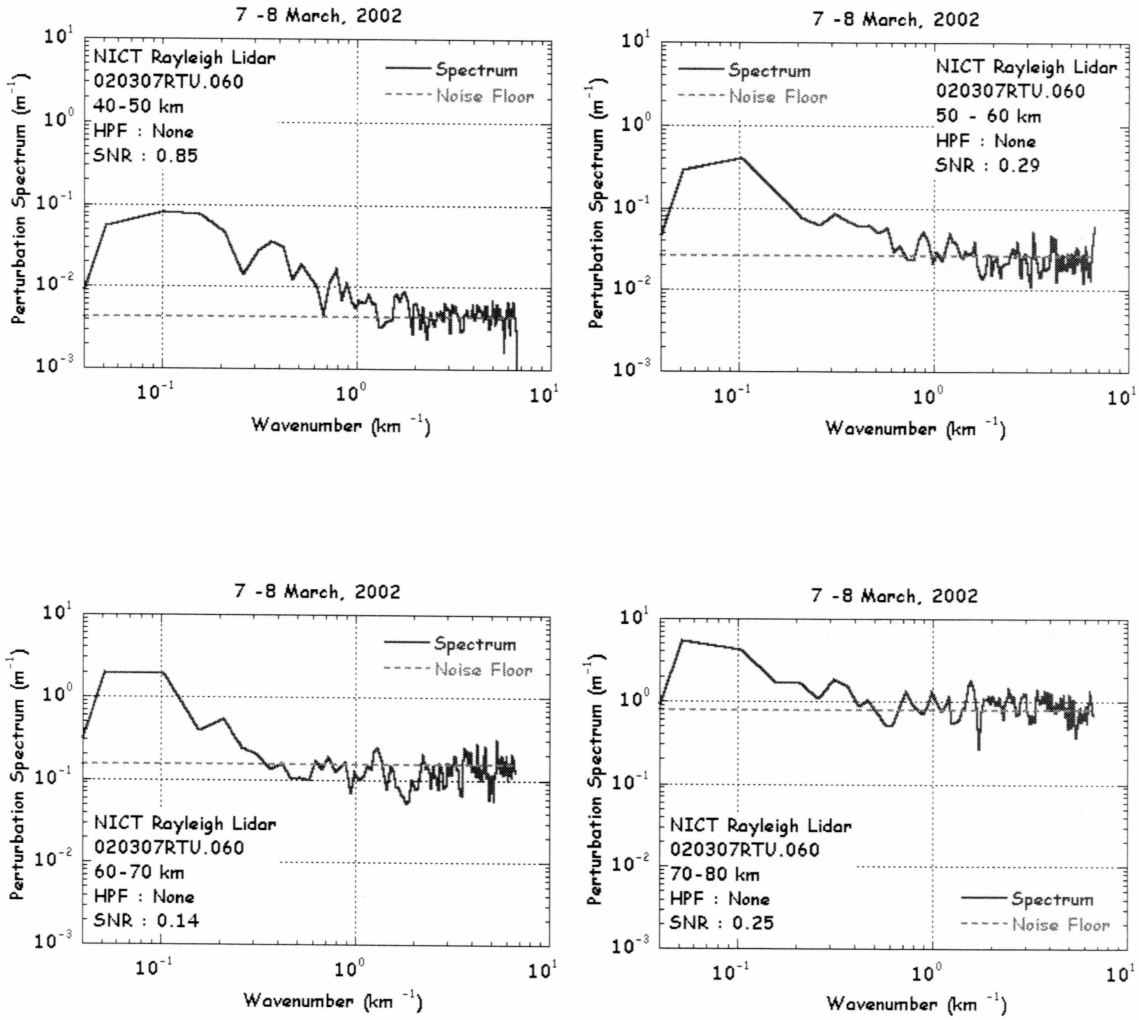

Figure 3.3: Average relative temperature perturbation spectra plotted as a function of wavenumber for different altitude ranges. Each spectrum represents the average of 11 individual spectra. (Upper left) 40-50 km altitude range. (Upper right) 50-60 km range. (Lower left) 60-70 km. (Lower right) 70-80 km.

Table 3.2: Characteristics of temperature perturbation spatial spectra

Altitude Range	60-min			30-min			15-min		
	NFLR (dB)	SNRT	SNRC	NFLR (dB)	SNRT	SNRC	NFLR (dB)	SNRT	SNRC
40-50	-23.7	0.85	8.90	-20.5	0.54	5.49	-16.7	0.26	2.36
50-60	-15.8	0.29	4.35	-12.6	0.25	2.39	-9.0	0.15	1.30
60-70	-8.3	0.14	3.17	-4.9	0.03	2.06	-0.5	0.05	0.99
70-80	-1.1	0.25	1.78	4.1	0.17	1.87			

In Table 3.2 we also present the calculations of SNRC and SNRT for relative temperature perturbations calculated at 30-min and 15-min resolution. We see that as we increase the temporal resolution of the measurements, the noise floor increases. For a resolution change by a factor of two (i.e., 60-min to 30-min and 30-min to15-min) the noise floor increases by 3dB. As expected, we see that the signal-to-noise ratio, SNRT and SNRC, both decrease with an increase in resolution, and finally we see that at all resolutions (60-min, 30-min and 15-min) the effect of reducing the signal bandwidth from 6.67 km^{-1} to 0.5 km^{-1} is to increase the SNR by a factor of 10.

Section 3.5: Effect of Filtering

The duration of the Rayleigh lidar measurements varies with observation period. We only analyze observations that last longer than 4 h. While the minimum period is 4 h, the maximum period is highly variable and can be as long as 16 h. In order to avoid having different spectral components contribute to the power measured on different observation periods, we remove all components with periods longer than 4 h from the relative temperature perturbations. Furthermore, the filtering reduces sensitivity to

different background profiles as the differences in Figure 2.2 appear as a constant offset at each altitude. We remove the 4 h components by high-pass filtering the relative temperature perturbations in time with a brickwall filter with cutoff frequency of 0.25 h^{-1}. We now calculate the relative temperature perturbation spectra for the altitude ranges 40-50 km, 50-60 km, 60-70 km and 70-80 km. We plot the average spectra for each of the altitude ranges in the Figure 3.5. As in Figure 3.4, we find that each of the spectra have the same general characteristics as the average spectrum over the 40-80 km altitude region. They have a base-band component in the low-wavenumber region ($m < 0.5$ km^{-1}) and white noise component in the high-wavenumber region ($m > 5.5$ km^{-1}). We see in Figure 3.6 that the amplitude of the noise floor increases with increasing altitude range. For each of the spectra we calculate the noise floor, SNRT and SNRC, and tabulate these values in the Table 3.3. From Table 3.3, we see that the noise floor increases by 8 dB with an increase in 10 km altitude range. SNRC is approximately a factor of 10 greater than SNRT for altitudes up to 70 km.

Comparing Table 3.2 and Table 3.3, we see that the noise floor decreases by 3 dB for the 60-min data, 1.3 dB for the 30-min data and 0.6 dB for the 15-min data when the relative temperature perturbations are high-pass filtered. The decrease in noise floor is expected. When a signal with a resolution of 60-min and a Nyquist frequency of 0.5 h^{-1} is high-pass filtered with cutoff frequency 0.25 h^{-1}, the bandwidth is reduced from 0.5 h^{-1} to 0.25 h^{-1}. Thus the power associated with a white noise signal is reduced by half or 3dB. When a signal with a resolution of 30-min and a Nyquist frequency of 1 h^{-1} is high-pass filtered with cutoff frequency 0.25 h^{-1}, the bandwidth is reduced from 1 h^{-1} to 0.75 h^{-1}. Thus, the power associated with a white noise signal is reduced by a quarter or 1.2 dB. When a signal with a resolution of 15-min and a Nyquist frequency of 2 h^{-1} is high pass filtered with cutoff frequency 0.25 h^{-1}, the bandwidth is reduced from 2 h^{-1} to 1.75 h^{-1}. Thus, the power associated with a white noise signal is reduced by one eighth or 0.6 dB.

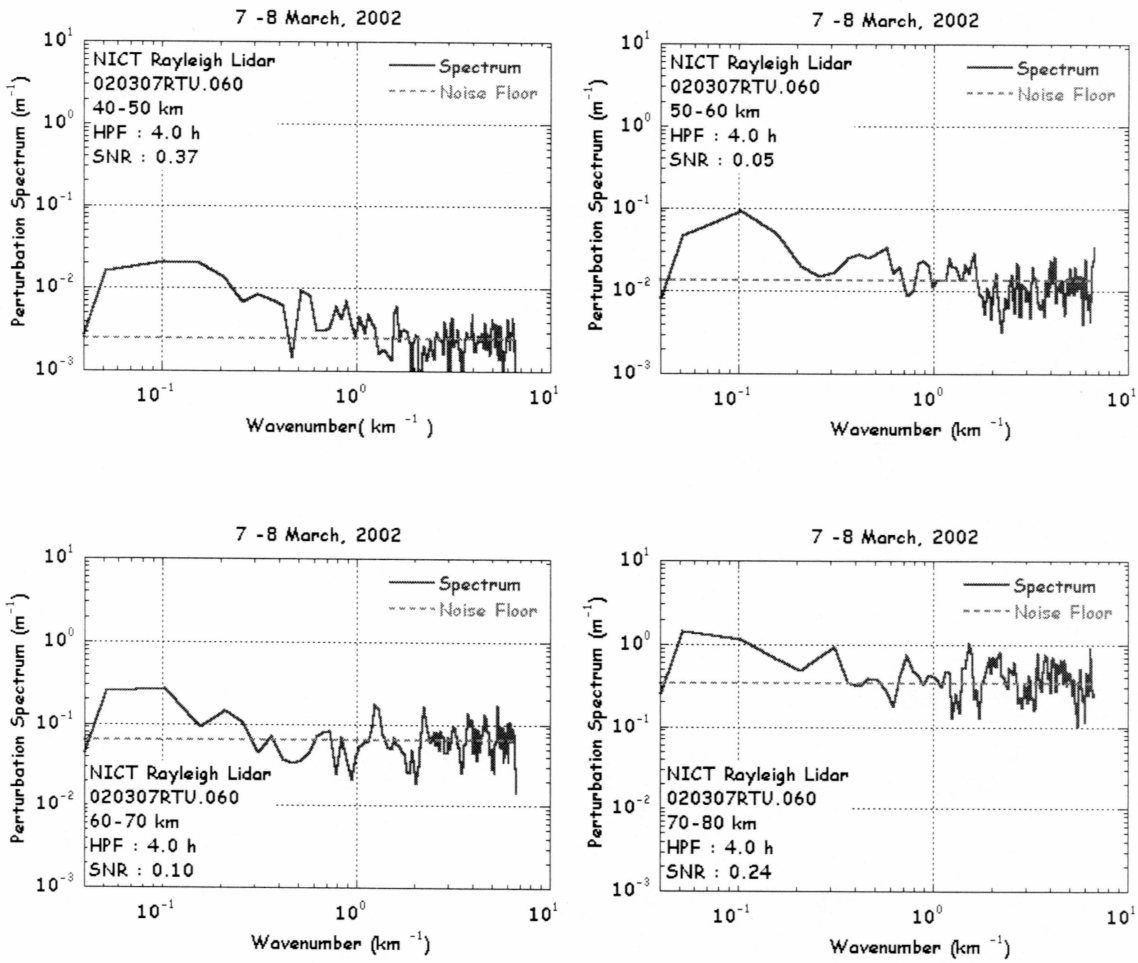

Figure 3.4: Average relative temperature perturbation spectra plotted as a function of wavenumber. For different altitude ranges the temperature perturbations have been temporally high-pass filtered with a cutoff of 0.25 h^{-1}. (Upper left) 40-50 km altitude range. (Upper right) 50-60 km range. (Lower left) 60-70 km. (Lower right) 70-80 km.

These white noise estimates agree with the noise floor measurements in Table 3.3 and confirm the fact that the instrumental noise acts as an additive white noise. However, we also see that the high-pass filtering reduces the signal-to-noise ratios, SNRT and SNRC, by approximately two.

Table 3.3: Characteristics of temperature perturbations spatial spectra with temporal filtering

Altitude Range	60-min			30-min			15-min		
	NFLR (dB)	SNRT	SNRC	NFLR (dB)	SNRT	SNRC	NFLR (dB)	SNRT	SNRC
40-50	-26.09	0.37	3.56	-21.58	0.28	2.50	-17.18	0.15	1.09
50-60	-18.64	0.05	1.54	-13.87	0.12	0.68	-9.54	0.08	0.48
60-70	-11.93	0.10	0.82	-6.44	0.01	0.93	-1.24	0.04	0.46
70-80	4.69	0.24	1.09	2.29	0.22	1.89			

We see that the SNRs associated with the lidar measurements in Table 3.2 and Table 3.3 are low, being less than 1 in SNRT and less than 10 in SNRC. While the spectral calculations with brickwall spatial cutoff at $m_c = 0.5$ km^{-1} yield measurements of SNRC, the filtered data will exhibit significant Gibbs phenomena in the space-time domain. In order to reduce this effect, we smooth the photon count profiles with a 2-km running average before determining the temperature profiles and the relative temperature perturbations. We plot the sequence of relative temperature perturbations in Figure 3.5 using unsmoothed (upper panel) and smoothed (lower panel) photon count data. In both cases the relative temperature perturbations are spatially filtered with a low-pass cutoff of 0.5 km^{-1} and high-pass filtered with a temporal cutoff of 0.25 h^{-1}. The Gibbs phenomenon is clearly observed as an oscillation of period of 2 km in the profiles in the upper panel of Figure 3.5. We plot the average spectra of temperature perturbations calculated from unsmoothed and smoothed photon count data in Figure 3.6. The effect of the photon count smoothing is to remove all spectral components at wavenumbers greater

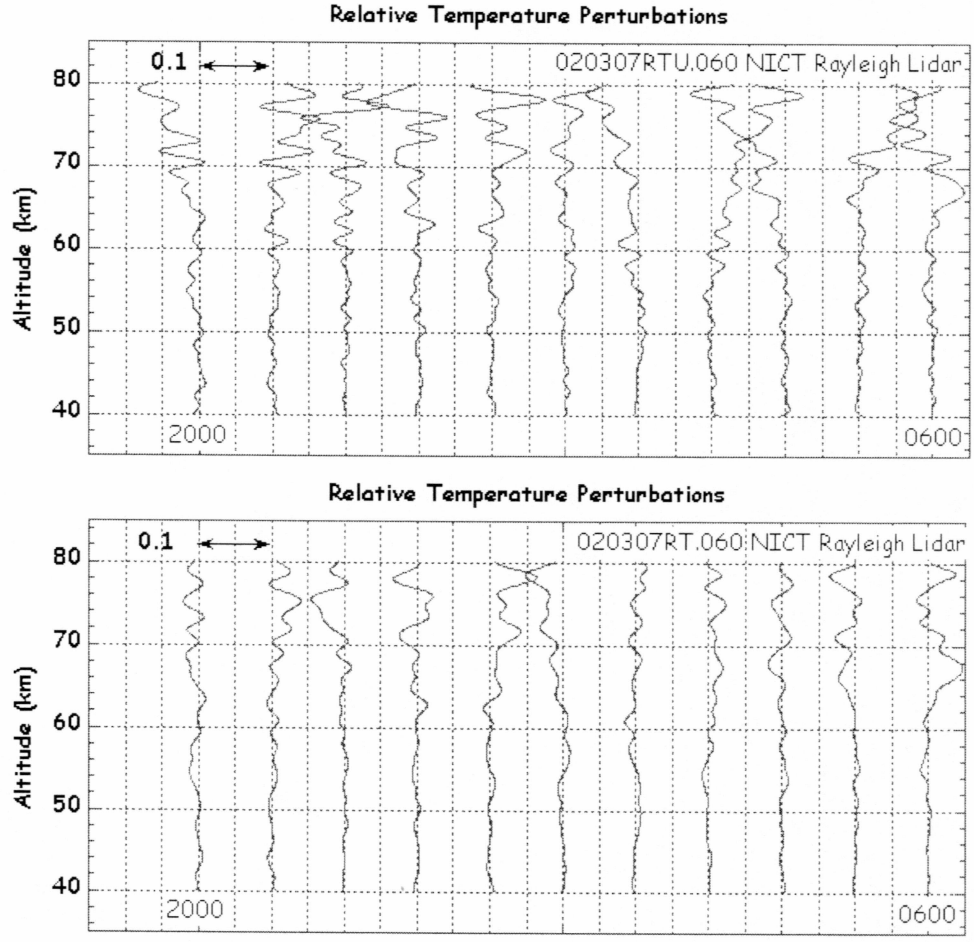

Figure 3.5: Sequence of relative temperature profiles plotted as a function of altitude. The profiles are calculated from 60-min temperature profiles. The successive profiles are offset by 0.1. The relative temperature perturbations are spatially low-pass filtered with a cutoff of 0.5 km^{-1} and temporally high-pass filtered with a cutoff of 0.25 h^{-1}. (Upper) The relative temperature profiles derived from photon counts that are not smoothed. (Lower) The relative temperature profiles derived from photon counts that are smoothed with a 2-km running average.

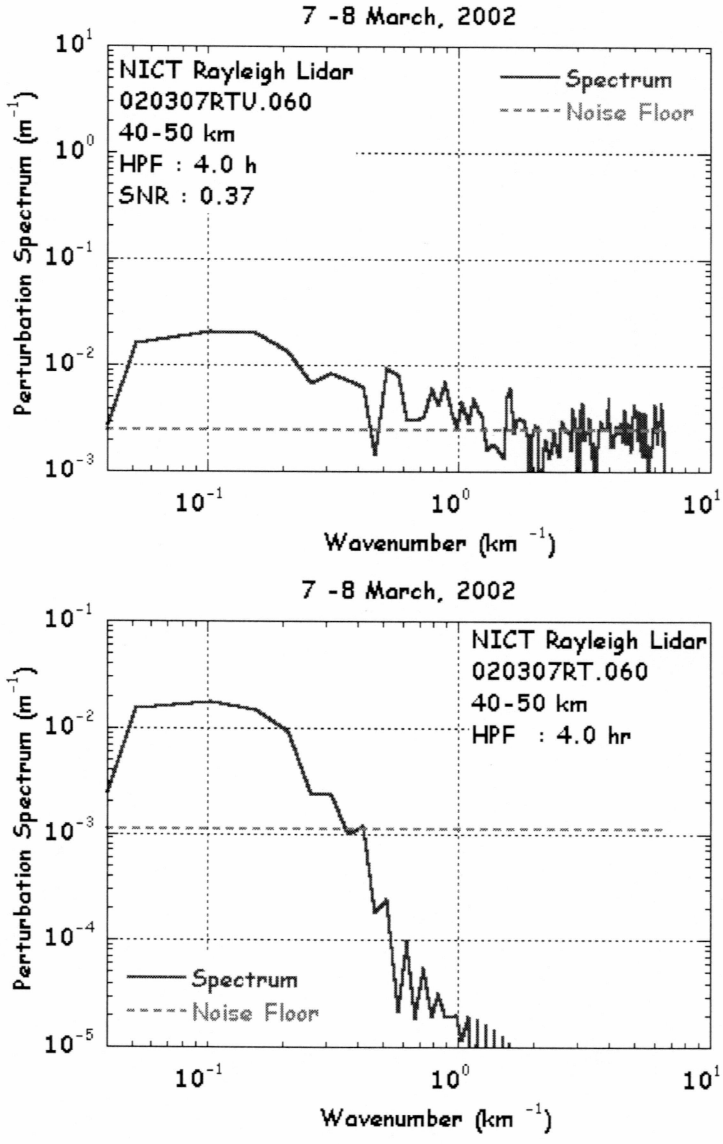

Figure 3.6: Average temperature perturbation spectrum plotted against wavenummber for the 40-50 km altitude region. (Upper) Temperature profile calculated from photon counts that are not smoothed. (Lower) Temperature profile calculated from photon counts that are smoothed with a running average of width 2 km.

than 0.5 km^{-1}. Consequently, we cannot determine the spectral noise floor for the smoothed photon count data.

In order to determine the noise contribution to the total power of the perturbations of the smoothed photon count profiles, we consider the effect of smoothing on a white noise process. We generate a sequence of n pseudo-random numbers, X, with a Normal (or Gaussian) Distribution, with zero mean and unit variance (i.e., N (0,1). We apply a running average with a length of 27 points, corresponding to 2 km, to yield a sequence X_{sm}. We then low-pass filter the smoothed sequence, X_{sm}, with a cutoff corresponding to 2 km (or 27 points) to yield a sequence X_{fil1}. We low-pass filter the original sequence, X, with a cutoff corresponding to 2 km (or 27 points) to yield a sequence X_{fil2}. We then determine the ratio of the power in X_{fil1} to X_{fil2}. The average of the ratios is calculated for both sets of 30 and 300 sequences of different lengths. We tabulate the results of the simulation in Table 3.4. For each trial we present the mean and relative standard deviation. The mean and relative standard deviation over three experiments is tabulated in Table 3.4. The ratio of X_{fil1} to X_{fil2} converges to 0.45. We use this result to calculate the noise power in relative temperature perturbation profiles where the photon counts have been smoothed at 2 km and the relative temperature perturbations have been filtered at 2 km, from unsmoothed and unfiltered perturbation data. We calculate the noise power for the smoothed and filtered data as,

$$N = N_{FLR} \times m_c \times 0.45 \tag{3.15}$$

where $m_c = 2\pi/2$ km^{-1} and N_{FLR} is calculated from unsmoothed and unfiltered data.

Table 3.4: Monte Carlo estimate of equivalent noise bandwidth

No. of iterations	No. of points	Trail 1		Trail 2		Trail 3	
		μ	σ (%)	μ	σ (%)	μ	σ (%)
30	4123	0.44	3.66	0.45	3.63	0.44	3.67
30	32795	0.45	0.86	0.45	0.86	0.45	0.81
30	65563	0.45	0.80	0.45	0.83	0.45	0.83
300	4123	0.45	2.78	0.45	2.78	0.45	2.77
300	32795	0.45	1.05	0.45	1.05	0.45	1.05
300	65563	0.45	0.74	0.45	0.74	0.45	0.74

Section 3.6: Variation of Total Power, Noise Power, Signal Power and SNR with Altitude

We can now use the spectral techniques developed to estimate the variation of total power, noise power, signal power and SNR with altitude. Using the estimated SNRs we can compare how the total power, signal power, and noise power estimates vary with altitude. We calculate the various power components and SNR from the average wavenumber spectra over the 40-50 km, 45-55 km, 50-60 km, 55-65 km and 60-70 km altitude ranges. We use the estimates of the noise power in the perturbations derived from unsmoothed photon count data to calculate noise power in the perturbations derived from the smoothed photon count data.

In Figure 3.7, we plot the altitude variations of the band-limited total power, signal power and noise power as well as SNR for relative temperature perturbations that are calculated from unsmoothed photon count data. We calculate the scale height of the power variations by fitting an exponential curve to the profiles $f(z) = f_o\, e^{-z/H}$. We see that SNRC has values between 2 and 10 over all altitude ranges and decreases with altitude as the noise power grows more rapidly with altitude than the signal power. The scale height of the signal power is 8.6 m, while that of the total power is 7.9 km and that of the noise is 5.5 km. In Figure 3.8, we plot the altitude variations of the band-limited total, signal and noise power as well as SNRC for relative temperature perturbations that have been have high-pass filtered with a cutoff of 0.25 h^{-1} and calculated from unsmoothed photon count data. We see that the effect of the high-pass filter is to reduce the signal power by a factor of approximately three. We see that SNRC has values between 0.6 and 4 over all altitude ranges and decreases with altitude as the noise power grows more rapidly with altitude than the signal power. The scale height of the signal power, H_S, is 12.9 km while that of the total power, H_P, is 8.5 km and that of the noise, H_N, is 6.0 km. In Figure 3.9, we plot the altitude variations of the band-limited total, signal and noise power as well as SNRC for relative temperature perturbations that have been have high-pass filtered with a cutoff of 0.25 h^{-1} and low-pass filtered with a cutoff of 0.5 km^{-1} and calculated from unsmoothed reduced by a factor of 0.45. The SNRC has values between 0.5 and 5 over all altitude ranges and decreases with altitude as the noise power grows more rapidly with altitude than the signal power. The scale height of the signal power is 12.3 km while that of the total power is 9.1 km and that of the noise is 6.0 km. We present these results in Table 3.5. All scale heights are in km. Unsmoothed and Smoothed refer to the photon counts, if they are unsmoothed or smoothed respectively.

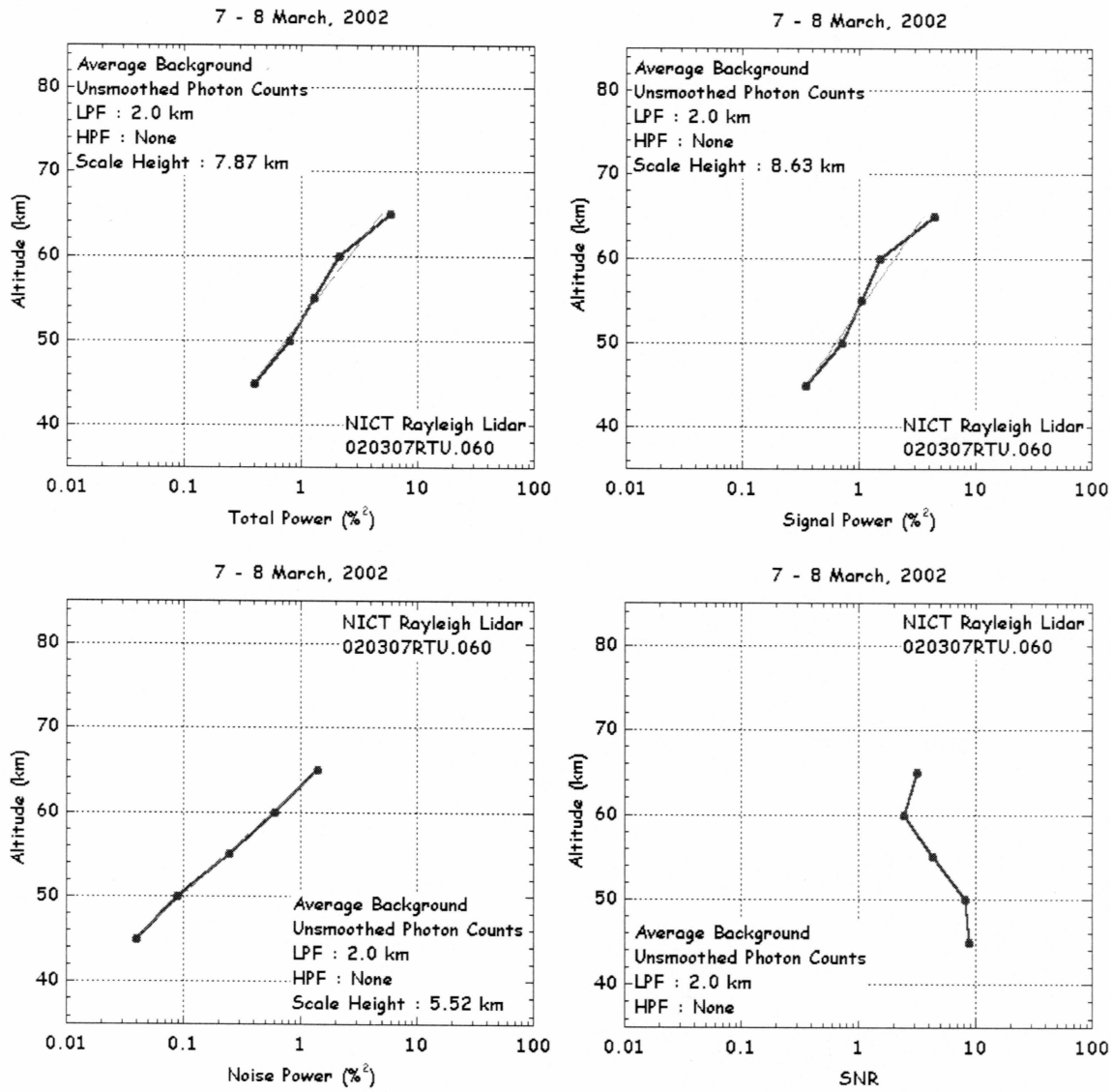

Figure 3.7: Variation of the total power (Upper left), signal power (Upper right), noise power (Lower left) and SNR (Lower right) with altitude. The power is calculated over 10 km intervals and plotted at the center of each interval. The perturbations are derived from 60-min unsmoothed photon counts.

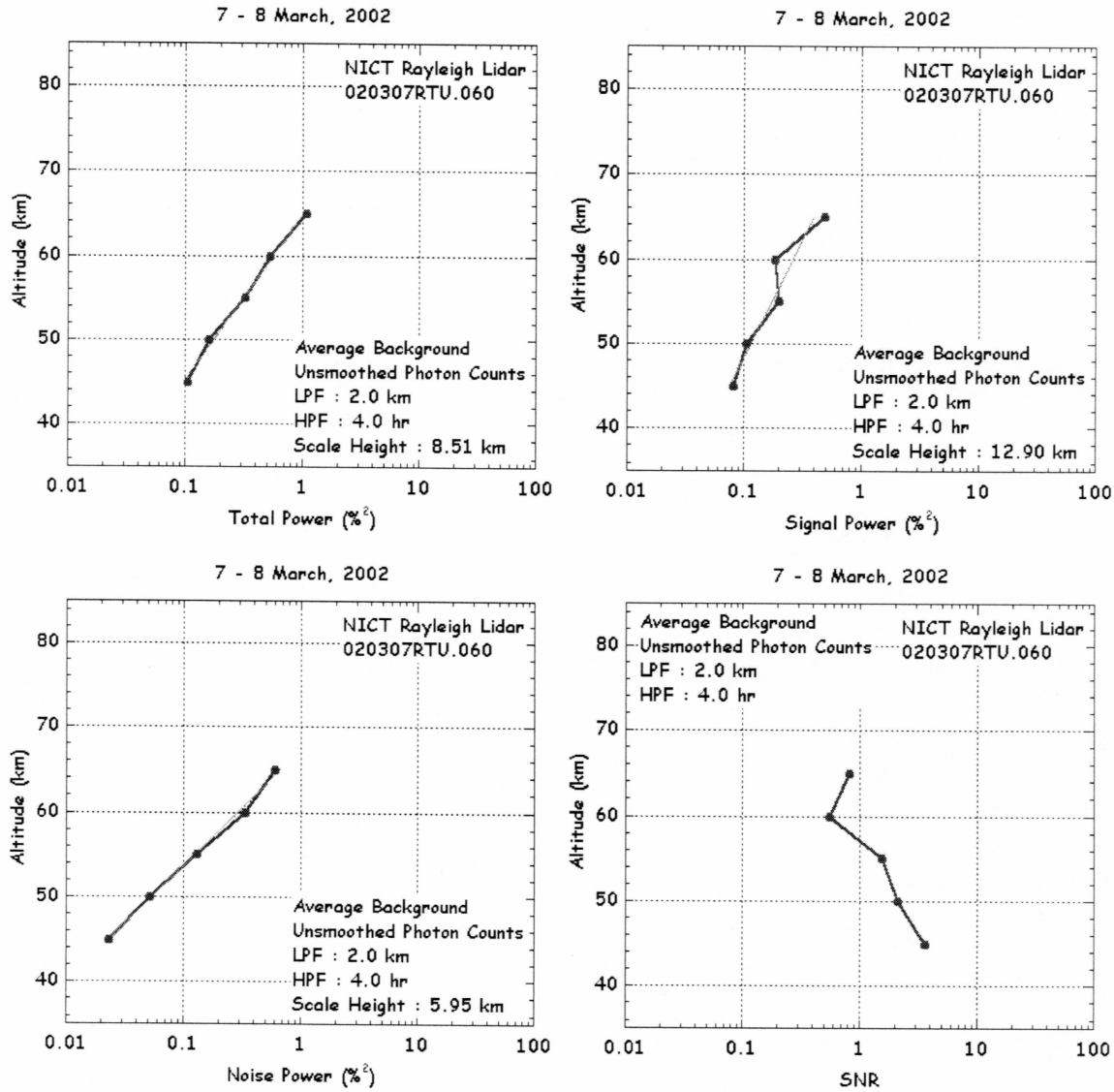

Figure 3.8: Variation of the total power (Upper left), signal power (Upper right), noise power (Lower left) and SNR (Lower right) with altitude. The power is calculated over 10 km intervals and plotted at the center of the interval. The perturbations are derived from 60-min unsmoothed photon count of March 7-8, 2002. The perturbations are temporally filtered with a cutoff at 0.25 h^{-1}.

The 2-km LPF refers to low-pass spatial filtering of photon count data. We see that the effect of the low-pass filter is to further reduce the signal power by a factor of approximately 1.25. The 4-h HPF refers to high-pass temporal filtering of perturbations with a cutoff of 0.25 h^{-1}.

We plot the sequence of relative temperature profiles at 30-min resolution in Figure 3.10. The Gibbs phenomenon is clearly observed in the relative temperature perturbations derived from unsmoothed photon counts. Oscillations of period 2 km in the profiles in the upper panel of Figure 3.10 can be observed. The relative temperature perturbations derived from smoothed photon counts are plotted in lower panel of Figure 3.10. The oscillations are not pronounced in these perturbation profiles, but downward phase progressions can be identified at 45 km at 2000 LST, 53 km at 2130 LST, at 48 km at 0000 LST and 48 km at 0400 LST. The gravity-wave activity observed are easily identified from the perturbation profiles derived from the smoothed photon counts rather than compared to the perturbation profiles derived from the unsmoothed photon counts. Therefore, smoothing the photon counts with a cutoff at 0.5 km^{-1} prevents oscillations that obscure the wave activity due to mathematically induced artificial oscillations.

We also tabulate the results of the analysis of the 30-min and 15-min relative temperature perturbations in Table 3.5. The higher resolution data yields lower values of SNRC and the scale heights determined for the signal power are closer to the noise power scale heights. These results suggest that we should apply caution in interpreting the altitude variation of the gravity-wave activity from these high-resolution measurements where SNRC is close to or less than one.

Section 3.7: Conclusion

We have analyzed the characteristics of the spatial periodogram and autocorrelation functions of the relative temperature perturbation profiles. We see that the lidar signal is composed of a base-band ($m \leq 0.5$ km^{-1}) geophysical signal and a white noise instrumental noise signal in the spatial domain. We find that the noise power for

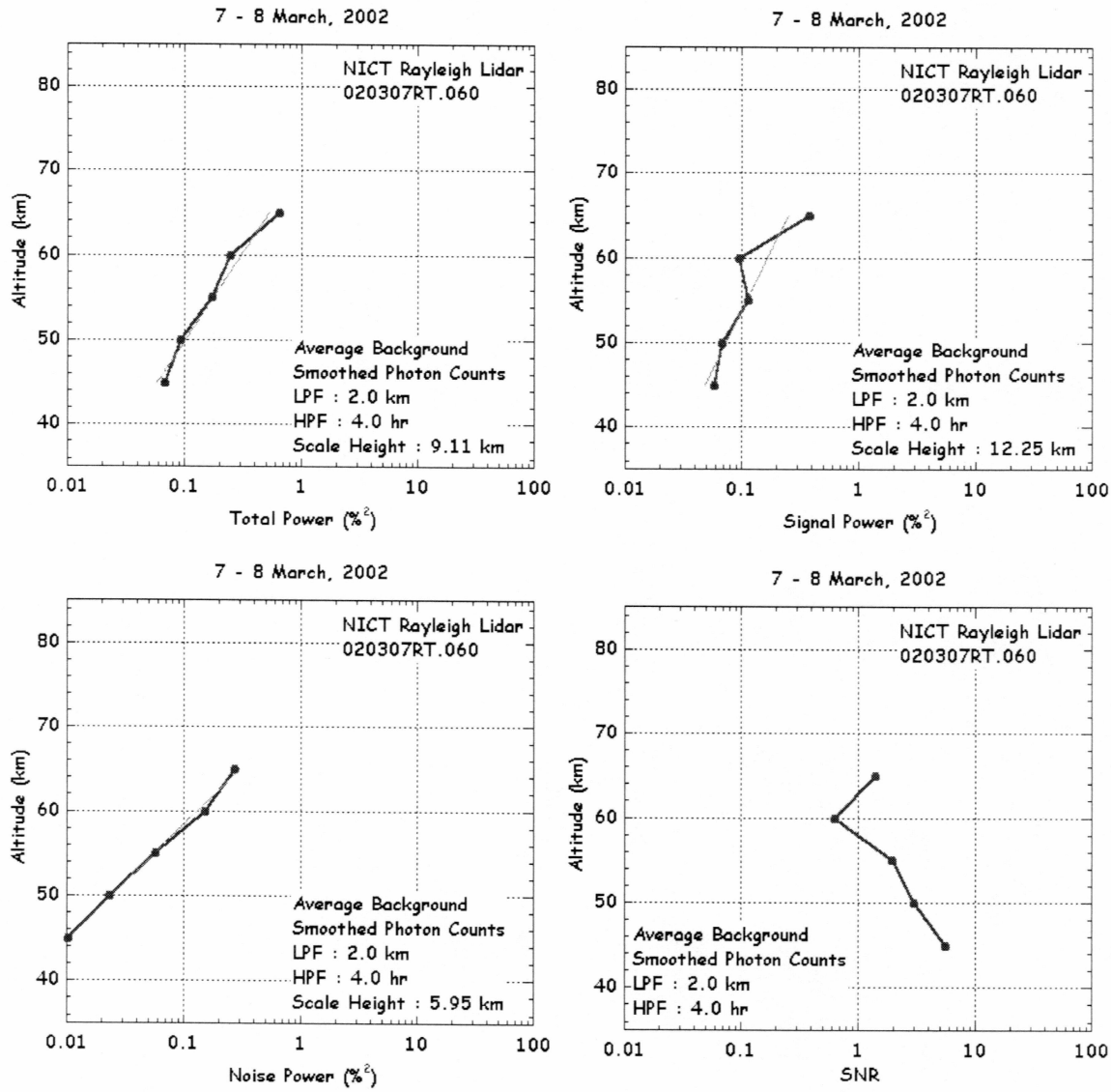

Figure 3.9: Variation of the total power (Upper left), signal power (Upper right), noise power (Lower left) and SNR (Lower right) with altitude. The power is calculated over 10 km intervals and plotted at the center of each interval. The perturbations derived are from 60-min smoothed photon count of March 7-8, 2002. The perturbations are temporally filtered with a cutoff at 0.25 h.

Table 3.5: Scale heights for relative temperature perturbation

Case	60-min			30-min			15-min		
	Total Power H_P(km)	Signal Power H_S(km)	Noise Power H_N(km)	Total Power H_P(km)	Signal Power H_S(km)	Noise Power H_N(km)	Total Power H_P(km)	Signal Power H_S(km)	Noise Power H_N(km)
Unsmoothed 2.0 km LPF	7.87	8.63	5.52	7.28	8.10	5.56	6.27	7.01	5.43
Unsmoothed 2.0 km LPF 4.0 h HPF	8.51	12.90	5.95	6.72	7.65	5.73	5.86	6.20	5.53
Smoothed 2.0 km LPF 4.0 h HPF	9.11	12.25	5.95	9.11	7.10	5.73	6.33	7.17	5.53

measurements (i.e., halving the bandwidth halves the noise power) of different temporal resolution scales, with the bandwidth of the measurements indicating a white noise behavior in the temporal domain. The spectral analysis allows us to determine the total power, the signal power, the noise power and the SNR. We have analyzed the variation of power with altitude and find that, where the SNR is high, the altitude variation of signal power has a significantly different scale height (~12.9 km) than that of the noise power (~6.0 km). We find that where the SNR is low, there is not a significant difference in the scale heights of the signal power (~ 7.1 km) and noise power (~5.7 km).

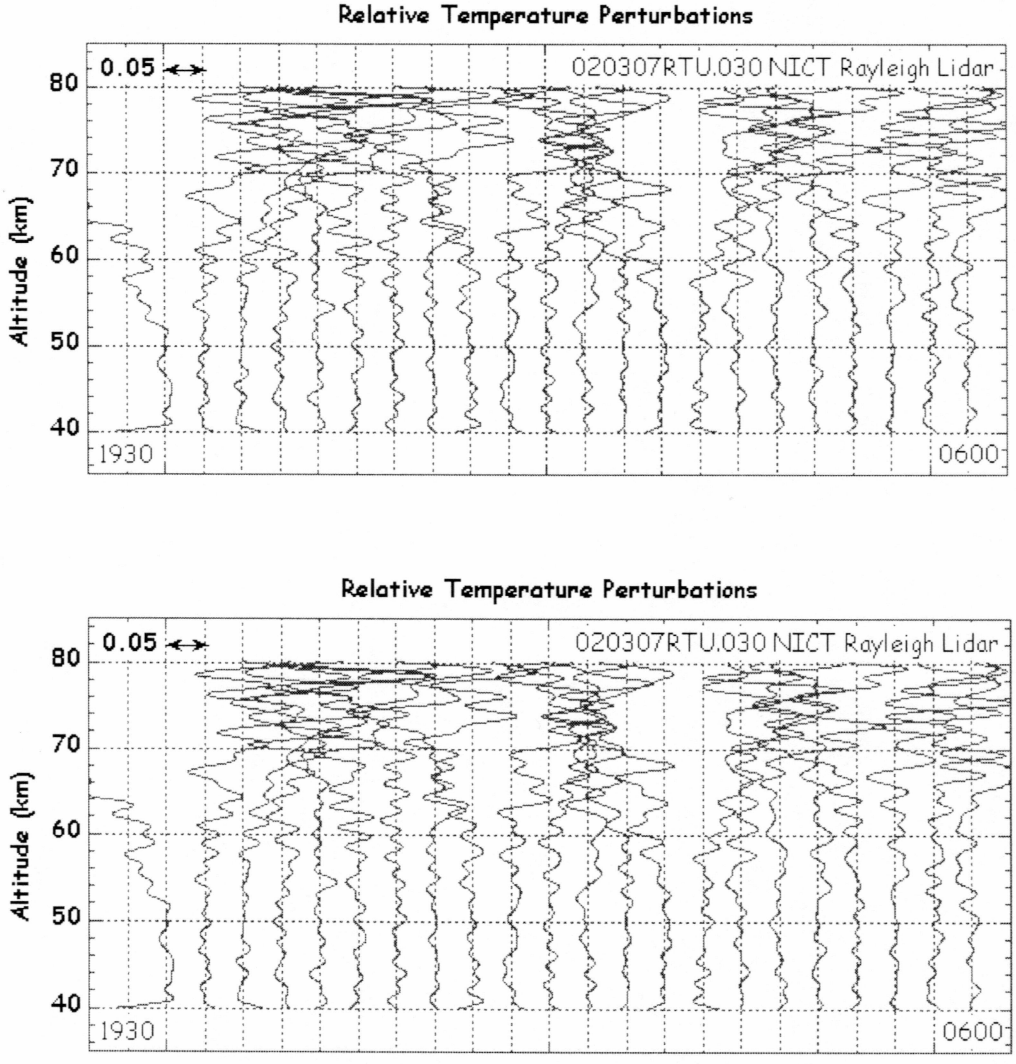

Figure 3.10: Sequence of relative temperature profiles plotted as a function of altitude. The profiles are calculated from 30-min temperature profiles. The successive profiles are offset by 0.05. The relative temperature perturbations are spatially low-pass filtered with a cutoff of 0.5 km^{-1} and temporally high-pass filtered with a cutoff at 0.25 h^{-1}. (Upper) The relative temperature profiles are derived from photon counts that are not smoothed. (Lower) The relative temperature profiles are derived from photon counts that are smoothed with a 2-km running average.

Chapter 4. Estimation of Signal and Uncertainties

Section 4.1: Introduction

In this chapter we determine the geophysical and instrumental uncertainties in the estimation of the signal and noise power. The uncertainties have been evaluated for 15, 30 and 60-min resolution for the 40-50 km, 50-60 km and 60-70 km altitude ranges. To illustrate the methods, we again use the measurements of March 7-8, 2002. We use the techniques described by Wang [2003] to calculate the temperature profiles at 60-min, 30-min and 15-min resolution. The background and dark counts are estimated from the lidar signal at 225 km. The photon counts are corrected for extinction. We use the techniques described in Chapter 2 to calculate relative temperature perturbations. The background profile is the average profile, computed by averaging the individual temperature profiles over the observation period. The relative temperature perturbations are temporally band-limited by the Nyquist frequency and a low frequency of 0.25 h^{-1} (corresponding to a period of 4 h). We choose the low frequency band limit to prevent variable contributions from long-period waves and tides to the perturbation power due to variations in the observation length.

Section 4.2: Geophysical and Instrumental Uncertainties

We estimate the uncertainties in the total, signal and noise power using three distinct methods:

i. We determine the variability in the signal and noise power estimates from the wavenumber spectra of individual perturbation profiles,

ii. We determine the variability in noise power estimates from the average wavenumber spectrum for the observation period,

iii. We determine the variability in the signal power from the space-time perturbations of appropriately filtered perturbations.

We then compare the relative uncertainties in these estimates to determine the most robust methods of analyzing the lidar data.

i. Sequence of spectra of individual perturbation profiles

The photon count profiles are not smoothed and the spectral noise floor extends to the Nyquist wavenumber. We determine the total base-band power, P_c, for each of the perturbation spectra, $S(i,k)$, as

$$P_c(i) = \sum_k S(i,k) \cdot \Delta m \tag{4.1}$$

where the index, k, is summed over the bandwidth where the wavenumber, m, is less than 0.5 km^{-1} band limit and Δm is the wavenumber resolution of the perturbation spectrum. We determine the average power, P, for the observation period as the sample mean of the $n1$ power estimates in time,

$$P = \frac{1}{n1} \sum_{i=1}^{n1} P_c(i) \tag{4.2}$$

The uncertainty in the average power estimate ΔP is computed as the uncertainty in a sample mean [e.g., Papoulis, 2002],

$$\Delta P = \sqrt{\frac{1}{n1 \times (n1-1)} \sum_{i=1}^{n1} (P_c(i) - P)^2} \tag{4.3}$$

The average total power in the perturbation, P, for the observations of March 7-8, 2002 at 60-min resolution is 0.131×10^{-4}, and the uncertainty in the power, ΔP, is 0.014×10^{-4}. Similarly, we calculate the average noise power, N, and the uncertainty in the noise power, ΔN, as follows,

$$N_{FLR}(i) = \frac{1}{nz} \sum_{k=nz1}^{nz2} S(i,k) \tag{4.4}$$

$$N_c(i) = N_{FLR}(i) \times nc \times \Delta m \tag{4.5}$$

$$N = \frac{1}{n1}\sum_{i=1}^{n1} N_c(i) \tag{4.6}$$

$$\Delta N = \sqrt{\frac{1}{n1 \times (n1-1)}\sum_{i=1}^{n1}(N_c(i)-N)^2} \tag{4.7}$$

where $N_{FLR}(i)$ is the noise floor of individual perturbation spectra, *nz1* and *nz2* are the wavenumber limits of the noise floor in the band 5.5 km^{-1} and 6.67 km^{-1}, *nz* (= *nz2-nz1+1*) is the number of points in the noise floor band and N_c is the noise power in 0.5 km^{-1} wavenumber base-band. The average noise power in the perturbations is 0.028×10^{-4} and uncertainty is 0.004×10^{-4}. We compute the average signal power, S, as sample mean of the signal power, $S_c(i)$, of each of the wavenumber spectra. The signal power $S_c(i)$ is the computed from the SNR of the 0.5 km^{-1} base-band, SNRC,

$$SNRC(i) = \frac{P_c(i) - N_c(i)}{N_c(i)} \tag{4.8}$$

$$S_c(i) = \frac{P_c(i)}{1 + \dfrac{1}{SNRC(i)}} \tag{4.9}$$

$$S = \frac{1}{n1}\sum_{i=1}^{n1} S_c(i) \tag{4.10}$$

$$\Delta S = \sqrt{\frac{1}{n1 \times (n1-1)}\sum_{i=1}^{n1}(S_c(i)-S)^2} \tag{4.11}$$

The estimated signal power is 0.103×10^{-4} and its uncertainty is 0.012×10^{-4}.

The total power, P_c, noise power, N_c, signal power, S_c, and SNR, SNRC are plotted as a function of time for the March 7-8, 2002 observation period in Figure 4.1. From Table 4.1, we see that the variation in the noise power is very much less than the

variation in the signal power. We conclude that the variability in the total power, and hence the signal power, represents the geophysical variability during the night.

ii. Average of perturbation spectra

We determine the total base-band power, P_{avg}, from the average perturbation spectrum, $S(k)$, as follows,

$$P_{avg} = \sum_{k} S(k) \cdot \Delta m \tag{4.12}$$

This estimate of the average total power, P_{avg}, is identical to the average of the total power of the individual spectra, P. We cannot determine the uncertainty, ΔP_{avg}, from the single average spectrum and we take the value, ΔP, as computed, in Eqn 4.3, from individual spectra. The noise power, N_{avg}, is computed similar to the N_c as follows

$$N_{FLRavg} = \frac{1}{nz} \sum_{k=nz_1}^{nz_2} S(k) \tag{4.13}$$

$$N_{avg} = N_{FLRavg} \times nc \times \Delta m \tag{4.14}$$

$$\Delta N_{avg} = \sqrt{\frac{1}{nz \times (nz-1)} \sum_{i=nz1}^{nz2} (S(k) - N_{FLRavg})^2} \tag{4.15}$$

We calculate the signal power, S_{avg}, as

$$S_{avg} = P_{avg} - N_{avg} \tag{4.16}$$

We compute the uncertainty in the signal power, ΔS_{avg}, as

$$\Delta S_{avg} = \sqrt{\Delta P_{avg}^2 + \Delta N_{avg}^2} \tag{4.17}$$

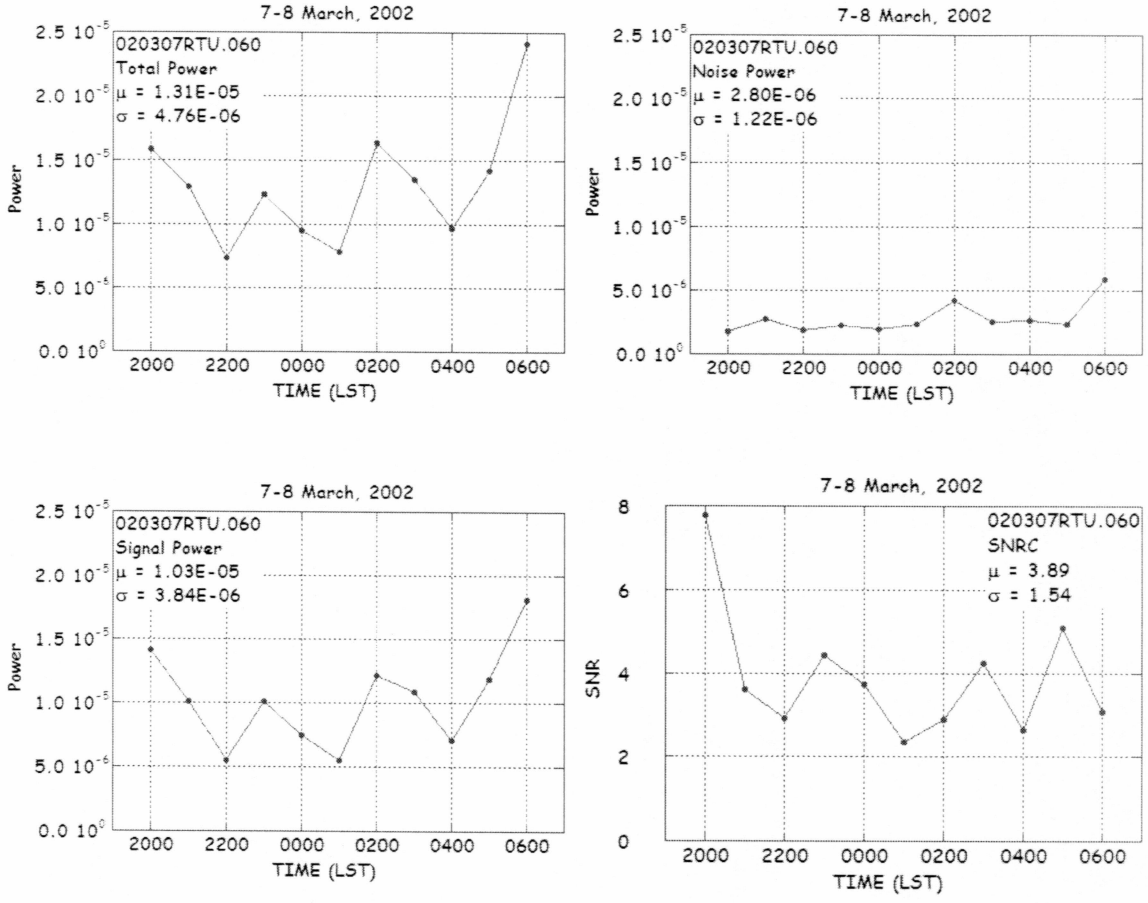

Figure 4.1: Total power, signal power, noise power and SNR in the 40-50 km altitude region plotted as function of observation time on the night of March 7-8, 2002. The power and SNR calculations are calculated from the 0.5 km^{-1} base band of individual spectra. (Upper left) Total power. (Upper right) Noise power. (Lower left) Signal power. (Lower right) Signal-to-Noise Ratio.

The power, noise power and signal power and their uncertainties are tabulated in Table 4.1. The noise floor of the average spectrum is 2.83×10^{-3} and has an uncertainty of 1.15×10^{-3}. We plot the average wavenumber spectrum in Figure 4.2. We also plot the spectrum of the 60-min profile at 0600 LST. Clearly the average spectrum is less variable than the 0600 LST spectrum. The perturbation spectrum at 0600 LST has a noise floor of 6.00×10^{-3} with an uncertainty of 6.78×10^{-3}. The relative uncertainty in the noise floor estimate for the average spectrum is 41%, the relative uncertainty in the 0600 LST spectrum is 113%, and the relative uncertainty due to the sample uncertainty in the average of the individual spectra is 110 %. Therefore, we choose the noise power estimated from the average spectrum over the one estimated from individual perturbation as a more robust estimate of the average noise power.

iii. Analysis of profiles in space and time

We filter the relative temperature perturbations with 2-km low-pass filter having computed the perturbations from photon count profiles that were smoothed with a 2-km running average. We calculate the average total power, P_{sm}, in the perturbation profiles, r_T', as the ms of the amplitude of the perturbations in altitude averaged over time,

$$P_{smi}(i) = \frac{1}{n2}\sum_{j=1}^{n2} r_T'(i,j)^2 \tag{4.18}$$

$$P_{sm} = \frac{1}{n1}\sum_{i=1}^{n1} P_{smi}(i) \tag{4.19}$$

We calculate the uncertainty in the average total power estimate, ΔP_{sm}, as the uncertainty

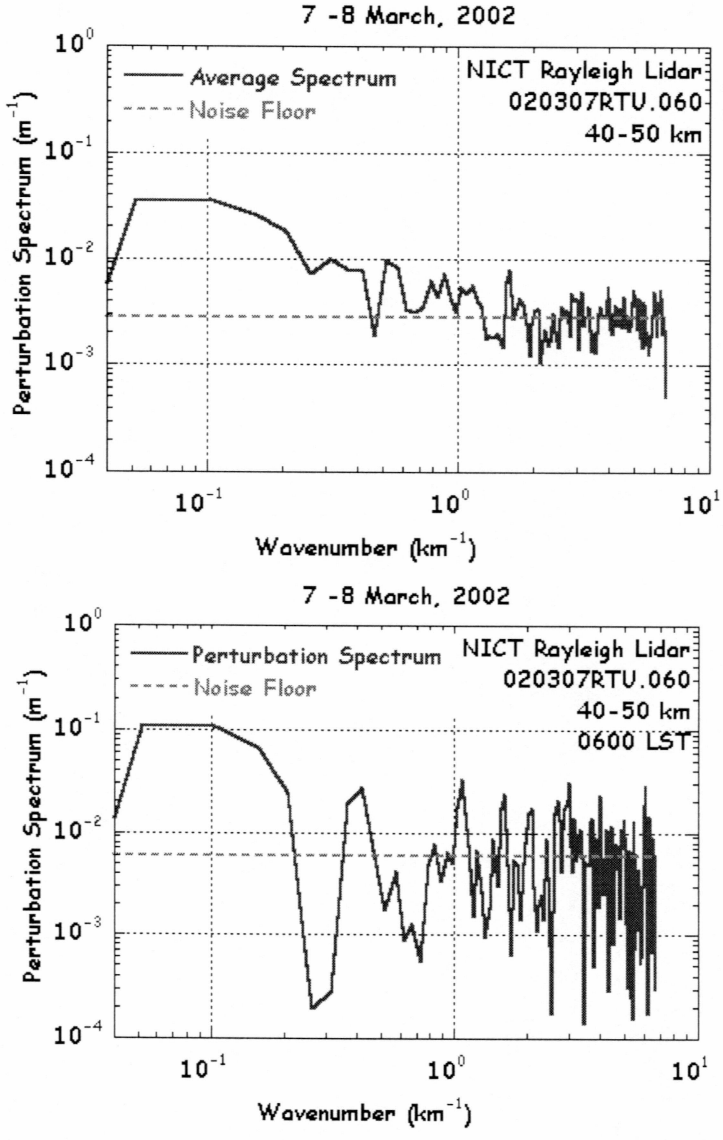

Figure 4.2: The spectrum(solid) and noise floor (dashed) plotted as a function of wavenumber. (Upper) The spectrum of average perturbation spectrum. (Lower) The spectrum of perturbation profile at 0600 LST.

in the sample mean over the n1 samples in time,

$$\Delta P_{sm} = \sqrt{\frac{1}{n1\times(n1-1)}\sum_{i=1}^{n1}(P_{smi}(i)-P_{sm})^2} \tag{4.20}$$

The power in the perturbation, P_{sm}, is 0.088×10^{-4}. The uncertainty in power, P_{σ}, is 0.014×10^{-4}. We calculate the noise power, N_{sm}, and uncertainty, ΔN_{sm}, from the average perturbation spectrum (using unsmoothed photon count data) as,

$$N_{sm} = N_{avg}\times0.45 \tag{4.21}$$

$$\Delta N_{sm} = \Delta N_{avg}\times0.45 \tag{4.22}$$

We calculate signal power, S_{sm}, in the perturbation as,

$$S_{sm} = P_{sm} - N_{sm} \tag{4.23}$$

We compute the uncertainty (or variability) in the signal power, ΔS_{sm}, as,

$$\Delta S_{sm} = \sqrt{\Delta P_{sm}^2 + \Delta N_{sm}^2} \tag{4.24}$$

We tabulate these power estimates in Table 4.1 with the associated relative uncertainties.

We examine the signal power in both the time-space domain and the wavenumber domain to determine the effect of Gibbs phenomena on our power estimates. The perturbation signal power is associated with gravity waves propagating in the atmosphere. Therefore, we correlate the signal power with the signatures of gravity waves to understand the physical mechanisms of gravity wave propagation in the middle atmosphere. In Figure 4.3 we plot the relative temperature perturbation profiles at 2000 LST and 0100 LST that are calculated from unsmoothed photon count profiles (thin) and smoothed photon count profiles (thick). The relative temperature profiles are low-pass filtered with a cutoff wavenumber of 0.5 km^{-1}. These profiles have the maximum (2000 LST) and minimum (0100 LST) values of SNRC (7.8 and 2.4 respectively) during the observation period. In Figure 4.3 we also plot the difference between the relative perturbation profiles calculated from unsmoothed photon count profiles and smoothed photon count profiles. The unsmoothed photon counts yield a ripple of 2-km in the

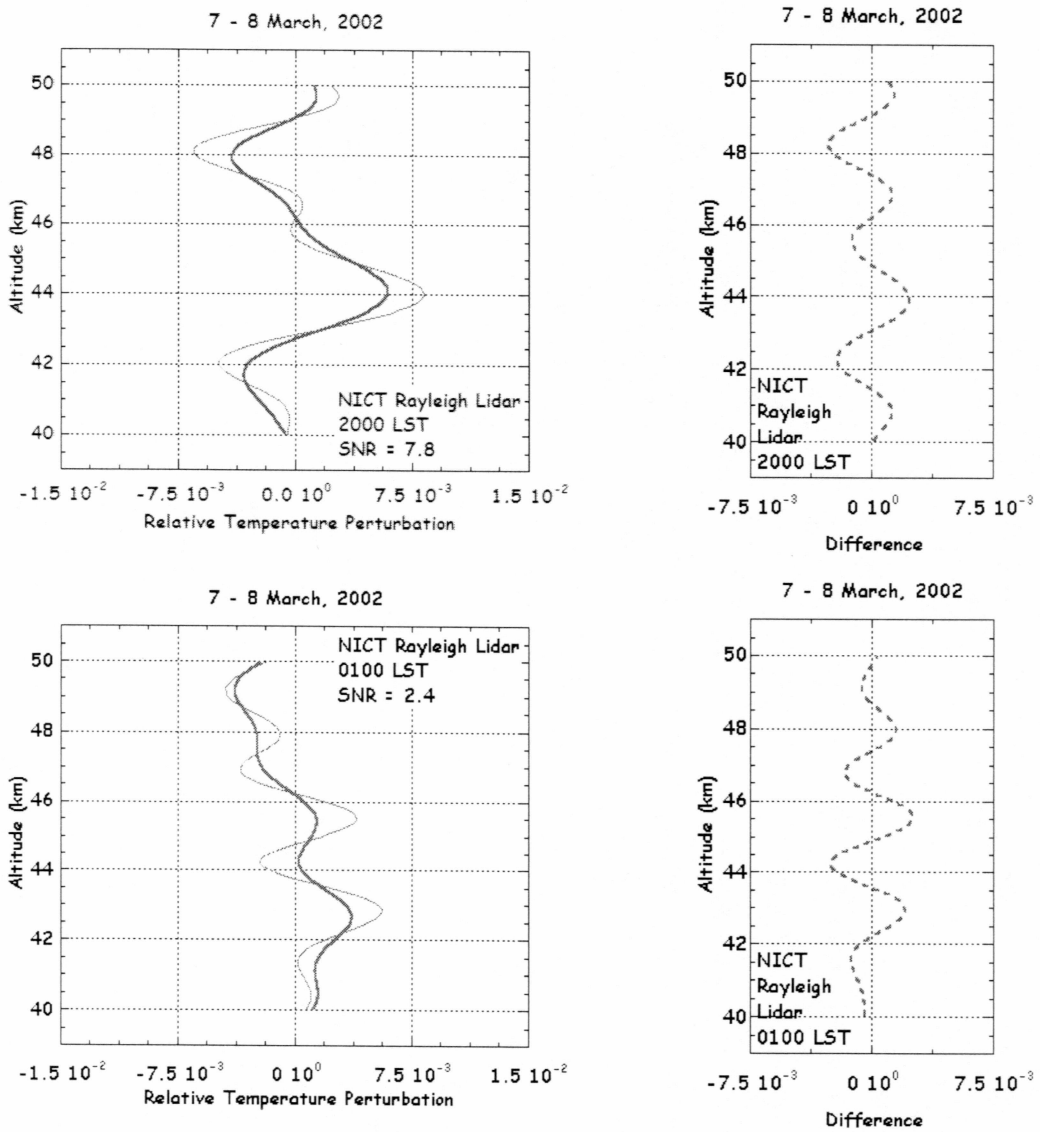

Figure 4.3: The relative temperature perturbation profiles plotted as a function of altitude for smoothed (thick) and unsmoothed (thin) photon counts. (Left) Relative temperature profiles at 2000 LST (upper) and 0600 LST (lower) on the night of 7-8 March 2002. (Right) The difference (dashed) between the unsmoothed and smoothed profiles.

relative temperature profiles that is superimposed on the large-scale perturbations in the profile. This 2-km ripple is clearly evident in the difference profiles (left) and more pronounced in the profile with lower SNR at 0100 LST. This 2-km ripple structure is due to Gibbs phenomenon. We conclude that rms amplitudes calculated from perturbations based on the unsmoothed photon count data yield an over-estimate of the signal power in the perturbations and give a distorted view of the wave activity.

We determine the uncertainties in the power estimates in two steps. We first estimate the uncertainty in the total power as the uncertainty in sample mean of the total power, in individual relative temperature perturbation profiles in space and in time. We then estimate the uncertainty in the noise power estimate as the uncertainty in the noise power estimate in the average temperature perturbation spectrum.

Table 4.1: Estimates of power with uncertainties in power

7-8 March, 2002, 60-min, 40-50 km

		Unsmoothed PC Individual Spectra	Unsmoothed PC Average Spectrum	Smoothed PC Spatial Profiles
P_c	μ[1]	0.131	0.131	0.088
	$\Delta\mu$[2]	0.014	0.014	0.014
	$\Delta\mu/\mu$[3]	0.110	0.110	0.162
S_c	μ	0.103	0.103	0.076
	$\Delta\mu$	0.012	0.015	0.014
	$\Delta\mu/\mu$	0.113	0.144	0.190
N_c	μ	0.028	0.028	0.013
	$\Delta\mu$	0.004	0.003	0.001
	$\Delta\mu/\mu$	0.132	0.123	0.107

1. μ is the estimate (10^{-4})
2. $\Delta\mu$ is the uncertainty in the estimate (10^{-4})
3. $\Delta\mu/\mu$ is the relative uncertainty

Section 4.3: Observations

We estimate the total power, signal power and noise power, using the three methods, for the 60-min data for six altitude ranges 40-50 km, 45-55 km, 50-60 km, 55-65 km, 60-70 km and 65-75 km altitude ranges. We tabulate the results in Table 4.2. The uncertainty in total power in method two is taken from method one . The mean and the uncertainty in the noise power in method three is taken from method two and scaled by a factor of 0.45 to compensate for the photon count smoothing. We see that as the total power and the noise power increases with altitude, both the geophysical uncertainty and the instrumental uncertainty in the estimates of the power also increase with altitude. We estimate the total power, signal power and noise power, using the three methods, for the 30-min data at six altitude ranges 40-50 km, 45-55 km, 50-60 km, 55-65 km, 60-70 km and 65-75 km. We tabulate the results in Table 4.3. Again, we see that as the total power and the noise power increases with altitude both the geophysical uncertainty and the instrumental uncertainty in the estimates of the power also increase with altitude. As we expect, the relative uncertainties in the signal power are larger for 30-min data than for the 60-min data. We estimate the total power, signal power and noise power, using the three methods, for the 15-min data at six altitude ranges 40-50 km, 45-55 km, 50-60 km, 55-65 km, 60-70 km and 65-75 km. We tabulate the results in Table 4.4. Again, we see that as the total power and the noise power increases with altitude, both the geophysical uncertainty and the instrumental uncertainty in the estimates of the power also increase with altitude. As we expect, the relative uncertainties in the signal power are larger for 15-min data than for the 30-min data and the 60-min data.

Section 4.4: Conclusion

We have analyzed the uncertainties in the power estimates of the relative temperature profiles. We have determined the most robust method for calculating the signal and noise power using a combination of spectral and time-space series analyses.

We find that as we increase the temporal resolution of the measurements and decrease the signal-to-noise ratio, the uncertainties in the power estimates increase. We also find that as altitude increases and the signal-to-noise ratio decreases, the uncertainties in the power estimates increase. This increase in uncertainty with altitude is reflected in both the geophysical and instrumental uncertainties.

Table 4.2: Power estimates and their uncertainties for 60-min data

		40-50	45-55	50-60	55-65	60-70	65-75
Sequence of spectra of individual perturbation profiles							
P_c	μ	0.131	0.197	0.361	0.594	2.413	4.772
	Δμ	0.014	0.042	0.062	0.081	1.363	2.243
	Δμ/μ	0.110	0.214	0.173	0.136	0.565	0.470
S_c	μ	0.103	0.137	0.211	0.202	1.649	3.122
	Δμ	0.012	0.038	0.054	0.066	1.215	2.003
	Δμ/μ	0.113	0.276	0.255	0.325	0.737	0.642
N_c	μ	0.028	0.060	0.150	0.391	0.763	1.650
	Δμ	0.004	0.005	0.027	0.055	0.152	0.285
	Δμ/μ	0.132	0.089	0.178	0.142	0.199	0.173
Average of perturbation spectra							
P_{avg}	μ	0.131	0.197	0.361	0.594	2.413	4.772
	Δμ	0.014	0.042	0.062	0.081	1.363	2.243
	Δμ/μ	0.110	0.214	0.173	0.136	0.565	0.470
S_{avg}	μ	0.103	0.137	0.211	0.202	1.649	3.122
	Δμ	0.014	0.042	0.063	0.083	1.363	2.245
	Δμ/μ	0.141	0.309	0.300	0.408	0.827	0.719
N_{avg}	μ	0.028	0.060	0.150	0.391	0.763	1.650
	Δμ	0.002	0.003	0.011	0.018	0.040	0.084
	Δμ/μ	0.061	0.057	0.071	0.047	0.052	0.051
Space-time analysis of temperature perturbation profiles							
P_{sm}	μ	0.088	0.114	0.179	0.283	1.847	2.322
	Δμ	0.014	0.024	0.032	0.060	1.397	1.387
	Δμ/μ	0.162	0.210	0.177	0.212	0.756	0.597
S_{sm}	μ	0.076	0.087	0.112	0.107	1.504	1.580
	Δμ	0.014	0.024	0.032	0.060	1.397	1.388
	Δμ/μ	0.189	0.276	0.287	0.566	0.929	0.878
N_{sm}	μ	0.013	0.027	0.068	0.176	0.343	0.743
	Δμ	0.001	0.001	0.005	0.008	0.018	0.038
	Δμ/μ	0.071	0.050	0.073	0.046	0.052	0.051

Table 4.3: Power estimates and their uncertainties for 30-min data

		Sequence of spectra of individual perturbation profiles					
		40-50	45-55	50-60	55-65	60-70	65-75
P_c	μ	0.240	0.325	0.666	1.627	4.706	13.85
	Δμ	0.021	0.048	0.110	0.255	1.282	3.522
	Δμ/μ	0.088	0.148	0.164	0.157	0.272	0.254
S_c	μ	0.169	0.151	0.249	0.630	2.350	7.723
	Δμ	0.021	0.040	0.093	0.251	1.173	2.710
	Δμ/μ	0.125	0.263	0.373	0.398	0.499	0.351
N_c	μ	0.070	0.174	0.417	0.997	2.356	6.127
	Δμ	0.006	0.017	0.039	0.069	0.211	0.976
	Δμ/μ	0.085	0.095	0.093	0.069	0.089	0.159
		Average of perturbation spectra					
P_{avg}	μ	0.240	0.325	0.666	1.627	4.706	13.85
	Δμ	0.021	0.048	0.110	0.255	1.282	3.522
	Δμ/μ	0.088	0.148	0.164	0.157	0.272	0.254
S_{avg}	μ	0.169	0.151	0.249	0.630	2.350	7.723
	Δμ	0.021	0.049	0.111	0.257	1.285	3.535
	Δμ/μ	0.125	0.322	0.443	0.407	0.547	0.458
N_{avg}	μ	0.070	0.174	0.417	0.997	2.356	6.127
	Δμ	0.003	0.007	0.014	0.028	0.084	0.296
	Δμ/μ	0.036	0.037	0.034	0.028	0.036	0.048
		Space-time analysis of temperature perturbation profiles					
P_{sm}	μ	0.131	0.172	0.371	0.824	3.195	8.996
	Δμ	0.016	0.042	0.097	0.193	1.400	4.644
	Δμ/μ	0.124	0.246	0.263	0.235	0.438	0.516
S_{sm}	μ	0.100	0.094	0.183	0.375	2.134	6.239
	Δμ	0.016	0.042	0.098	0.194	1.401	4.646
	Δμ/μ	0.164	0.452	0.533	0.516	0.656	0.745
N_{sm}	μ	0.032	0.078	0.188	0.449	1.060	2.757
	Δμ	0.001	0.003	0.006	0.013	0.038	0.133
	Δμ/μ	0.043	0.040	0.034	0.028	0.036	0.048

Table 4.4: Power estimates and their uncertainties for 15-min data

		Sequence of spectra of individual perturbation profiles				
		40-50	45-55	50-60	55-65	60-70
P_c	μ	0.379	0.603	1.611	4.203	11.586
	Δμ	0.041	0.061	0.384	1.161	4.530
	Δμ/μ	0.107	0.100	0.238	0.276	0.391
S_c	μ	0.183	0.078	0.485	1.293	3.860
	Δμ	0.028	0.097	0.232	0.517	2.196
	Δμ/μ	0.152	1.241	0.479	0.399	0.569
N_c	μ	0.196	0.525	1.126	2.910	7.725
	Δμ	0.029	0.112	0.171	0.723	2.481
	Δμ/μ	0.148	0.213	0.152	0.249	0.321
		Average of perturbation spectra				
P_{avg}	μ	0.379	0.603	1.611	4.203	11.586
	Δμ	0.041	0.061	0.384	1.161	4.530
	Δμ/μ	0.107	0.100	0.238	0.276	0.391
S_{avg}	μ	0.183	0.078	0.485	1.293	3.860
	Δμ	0.042	0.064	0.386	1.168	4.547
	Δμ/μ	0.229	0.820	0.795	0.903	1.178
N_{avg}	μ	0.196	0.525	1.126	2.910	7.725
	Δμ	0.011	0.021	0.039	0.134	0.402
	Δμ/μ	0.054	0.041	0.035	0.046	0.058
		Space-time analysis of temperature perturbation profiles				
P_{sm}	μ	0.240	0.360	0.829	1.728	5.921
	Δμ	0.066	0.089	0.274	0.488	2.402
	Δμ/μ	0.276	0.248	0.331	0.283	0.406
S_{sm}	μ	0.151	0.124	0.322	0.419	2.445
	Δμ	0.066	0.090	0.275	0.492	2.409
	Δμ/μ	0.438	0.726	0.852	1.175	0.985
N_{sm}	μ	0.088	0.236	0.507	1.310	3.476
	Δμ	0.005	0.009	0.018	0.060	0.181
	Δμ/μ	0.056	0.040	0.035	0.046	0.052

Chapter 5. Gravity Wave Activity at Chatanika

Section 5.1: Introduction

In this chapter, we estimate and compare the rms amplitudes in relative temperature and relative density perturbations for 89 observation periods. We have modified the density processing tools of Wang [2003] and developed methods to process the relative density perturbations in parallel with the temperature perturbation processing methods discussed in this thesis. The average density and temperature profile is used as the background profile for both sets of perturbations. We use the method described in Chapter 4 to compute the uncertainty in estimating the rms signal amplitude. The space-time analysis is used to determine the total power and the associated uncertainty. We use the average wavenumber spectrum to determine the noise power and the associated uncertainty. We then compare the results obtained from the temperature perturbations to those obtained by density perturbations to assess the gravity wave activity in the 40-50 km altitude region. All density and temperature perturbations are computed from the photon counts smoothed with a 2-km running average. The perturbations are then spatially filtered with a 2-km low-pass filter and filtered temporally with a cutoff at 0.25 h^{-1}.

Section 5.2: SNR of the Perturbations

The rms amplitude of signal and total uncertainty are computed for the 60-min, 30-min and 15-min data sets as explained earlier in Chapter 4. The observations are accumulated over 89 days of measurements made between November 14-15, 1997 and May 12-13, 2004. These observations were made in fall, winter and spring (i.e., early August through mid-May). The total number of profiles for the 60-min, 30-min and 15-min data is 763, 1450 and 2811, respectively. The number of profiles at each resolution are not simple multiples (ie., $1450 \neq 2\times763$, $2811 \neq 2\times1450$), as the observation may not have been made for the complete duration for which the photon count profile is integrated

[Wang, 2003]. The rms amplitude estimates are computed for the 40-50 km altitude range. The computations and statistics are presented in this chapter for days where the SNR (i.e., SNRC) is greater than one. For the temperature perturbations that are 4-h high-pass filtered, the mean SNR in 60-min data is 5.64 with a median of 4.02 over 80 days. For 30-min data, the average is 3.24 with a median of 2.50 over 67 days. For 15-min data, the mean SNR is 2.43 with a median of 1.75 over 49 days. For the density perturbations, the mean SNR for 60-min data is 5.30 with a median of 3.91 over 75 days. The average SNR for 30-min data is 2.78 with a median of 2.20 over 59 days and for 15-min data, the mean SNR is 2.13 with a median of 1.77 over 34 days The number of days with better SNR decreases with increasing resolution of the data. If the photon count profile is integrated in altitude, the quality increases to give a better SNR in temperature perturbations.

With the photon counts smoothed with a 2-km running average and the perturbations filtered with the 4-h high-pass filter and 2-km low-pass filter, the SNR in the temperature and density perturbations improve as expected. The SNR of the data is plotted in Figure 5.1 for the days when the SNR in both the perturbations is greater than one. With 60-min data, SNR is greater than 1 for 85 days out of 89 days. For the 30-min data, SNR is greater than one for 80 of 89 days, and for the 15-min data, 65 of 89 days. In the temperature perturbations, the mean SNR for the 60-min data over 85 days is 8.71 with a median of 5.77. In the 30-min data, the mean and median are 4.39 and 3.14, respectively. In the 15-min data, the mean and median are 3.00 and 2.31, respectively. Using density perturbations, the mean SNR in 60-min data is 8.85 with a median of 5.69. In the 30-min data, 4.39 and 3.09 are the mean and median, of SNR, respectively. In the 15-min data, the mean SNR is 2.96 with a median of 2.14. We summarize these results in Table 5.1. The SNR improved with resolution and smoothing. A maximum SNR of 43.87 is estimated from 60-min temperature perturbations on March 5-6, 2003.

Table 5.1: SNR of temperature and density perturbation measurements

		60-min		30-min		15-min	
		Tempe-rature	Density	Tempe-rature	Density	Tempe-rature	Density
Unsmoothed Photon Counts	Days	75	80	67	59	49	34
	Mean	5.30	5.64	3.24	2.78	2.43	2.13
	Median	3.91	4.02	2.50	2.20	1.75	1.77
Smoothed Photon Counts and Filtered perturbations	Days	85	85	80	80	65	65
	Mean	8.71	8.58	4.39	4.39	2.31	2.14
	Median	5.77	5.69	3.14	3.09	2.31	2.14

Section 5.3: Comparison of Relative Temperature and Density Perturbations

The average value of the ratio of uncertainty in power to uncertainty in noise, $\Delta P/\Delta N$, is about 70 in 60-min data, 38 in 30-min data and 35 in 15-min data. This indicates that the variability in signal power estimate is dominated by geophysical variability rather than instrumental uncertainty.

In Figure 5.4, Figure 5.5, and Figure 5.6 we plot the rms amplitude of the relative temperature signal against the relative density perturbations signal for 60-, 30- and 15-min data. We also plot the uncertainty in the estimation. Examining the 60-min data, for the 85 measurements where the SNR is greater than one, we find that the rms temperature perturbations are equal to the rms density perturbations within their uncertainties for all 85 measurements, i.e.,

$$rms_T - \Delta rms_T \le rms_D \le rms_T + \Delta rms_T \tag{5.1}$$

$$rms_D - \Delta rms_D \le rms_T \le rms_D + \Delta rms_D \tag{5.2}$$

Examining the 30-min data, for the 80 measurements where the SNR is greater than one, we find that the rms temperature perturbations are equal to the rms density perturbations

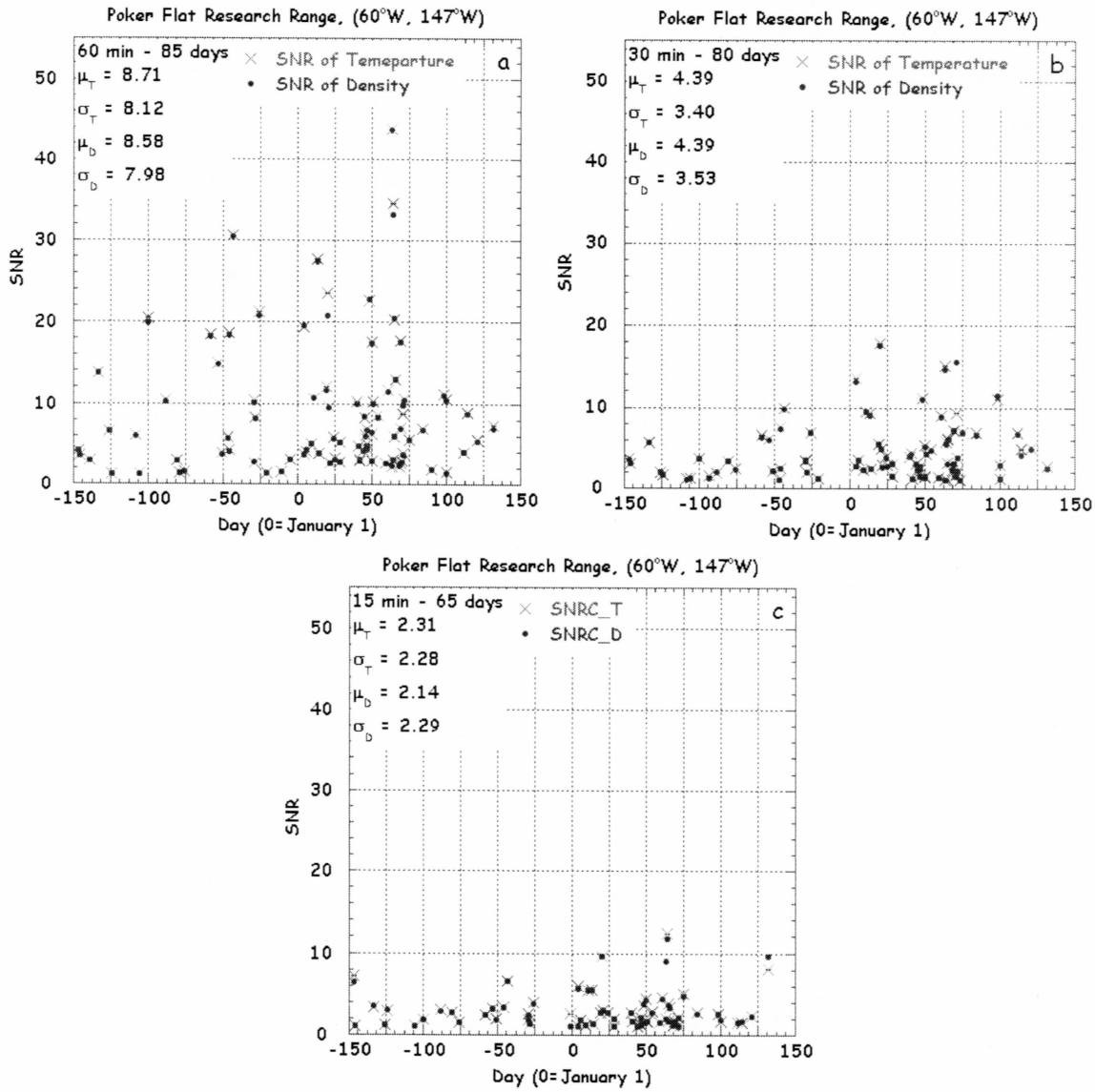

Figure 5.1: The SNR (i.e., SNRC) of the temperature and density perturbation measurement as a function of day number. (a) 60-min data. (b) 30-min data. (c) 15-min data.

within their uncertainties for all 80 measurements. Examining the 15-min data, for the 65 measurements where the SNR is greater than one, we find that the rms temperature perturbations are equal to the rms density perturbations within their uncertainties for 64 measurements.

For the 60-min data, the mean rms temperature perturbation is 0.38% with a standard deviation of 0.18% and we obtain identical values from the density perturbations. For the 30-min data the mean rms temperature perturbation is 0.47% with a standard deviation of 0.23% and and we obtain identical values from the density perturbations. For the 15-min data, the mean rms temperature perturbation is 0.57% with a standard deviation of 0.34% and the mean rms amplitude in the density perturbations is 0.56% with a standard deviation of 0.33%. Therefore, we conclude that the temperature perturbations and the density perturbations of the smoothed photon counts and filtered perturbations yield the same estimates of the rms gravity wave perturbations. The values of rms density and temperature perturbations are in good agreement with the observations of Gerrard and co-workers [Gerrard et al., 1998]. They report rms relative density perturbations of between 0.3% and 0.8% in the 30-45 km altitude range in August in Greenland.

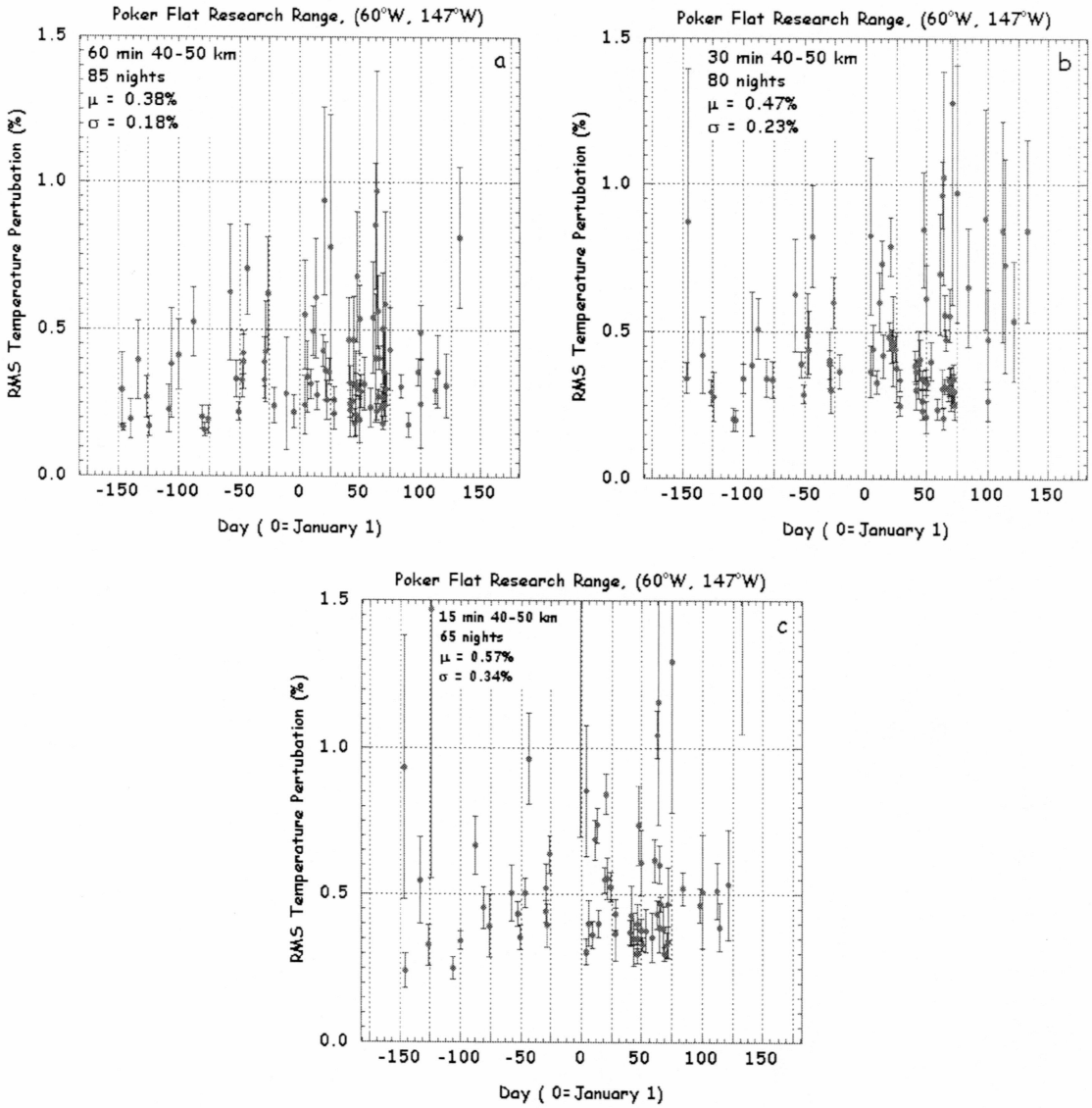

Figure 5.2: RMS amplitude of the relative temperature perturbations as function of day number. (a) 60-min data. (b) 30-min data. (c) 15-min data. The rms amplitude is computed using the third method described in Chapter 4.

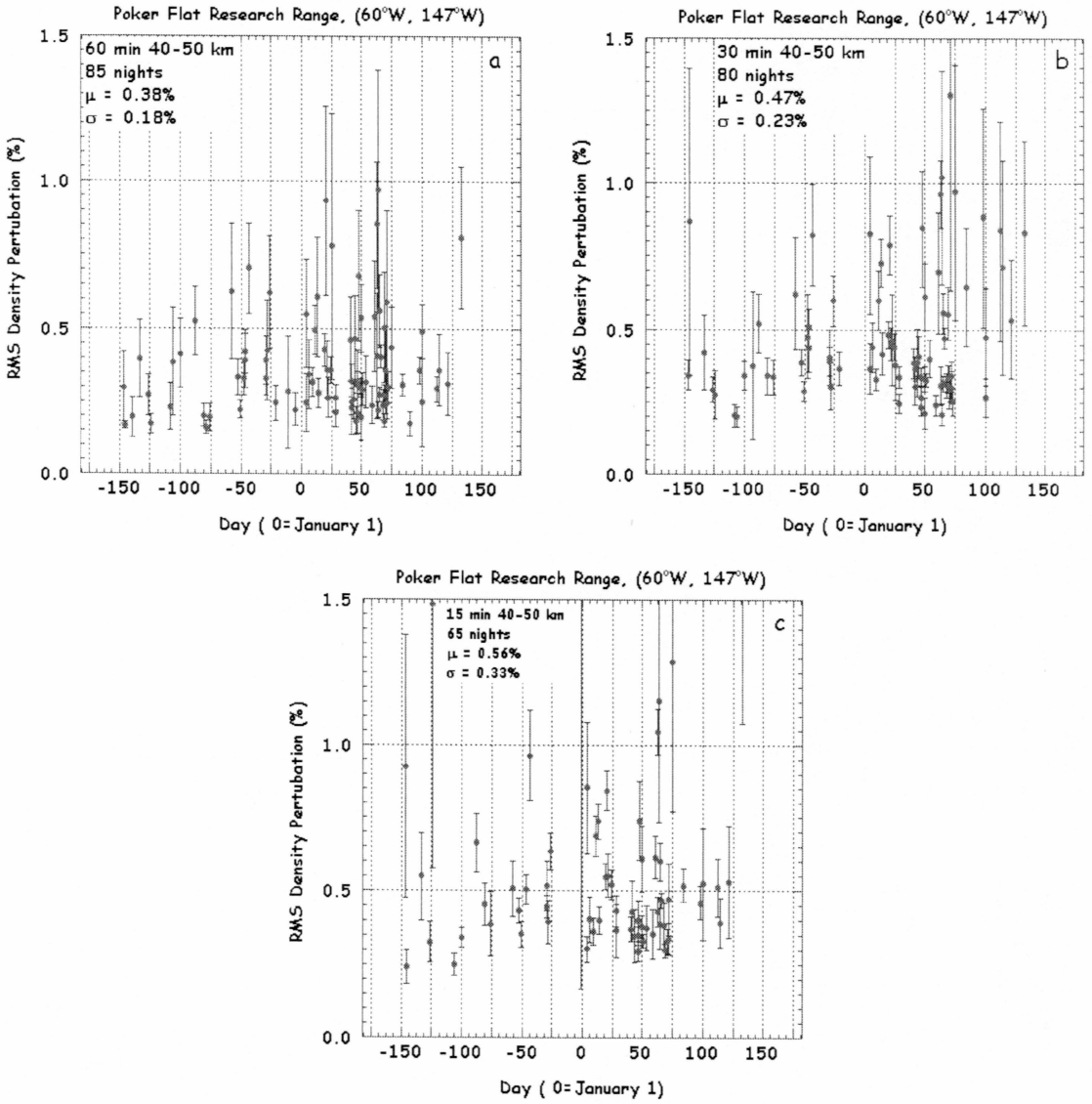

Figure 5.3: RMS amplitude of the relative density perturbations as function of day number. (a) 60-min data. (b) 30-min data. (c) 15-min data. The rms amplitude is computed using the third method described in Chapter 4.

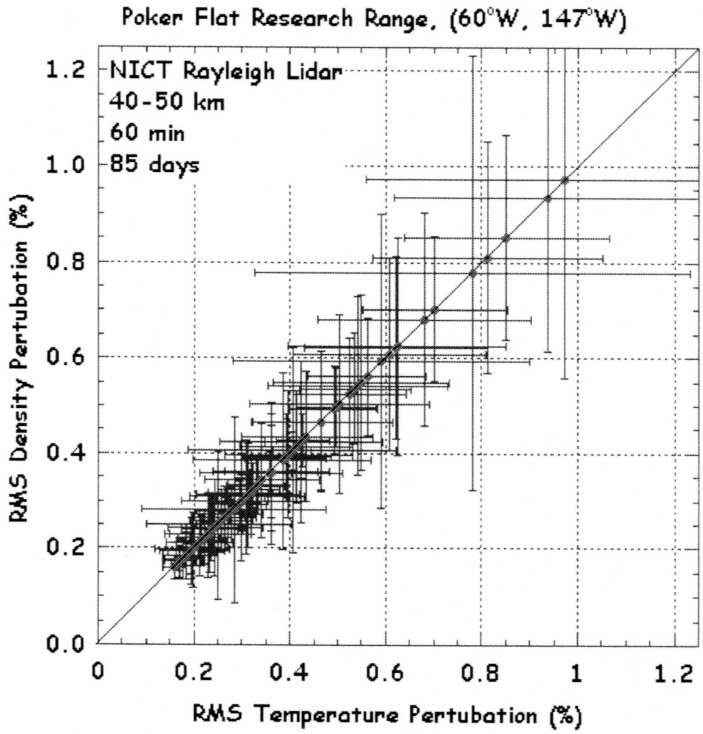

Figure 5.4: The rms signal amplitude of temperature plotted against density perturbations for 60-min data for 85 sets of observations. The nights chosen are those, when the SNR is greater than one in both density and temperature perturbations. The uncertainty in the rms amplitude estimation for each night is also plotted for temperature and density perturbations.

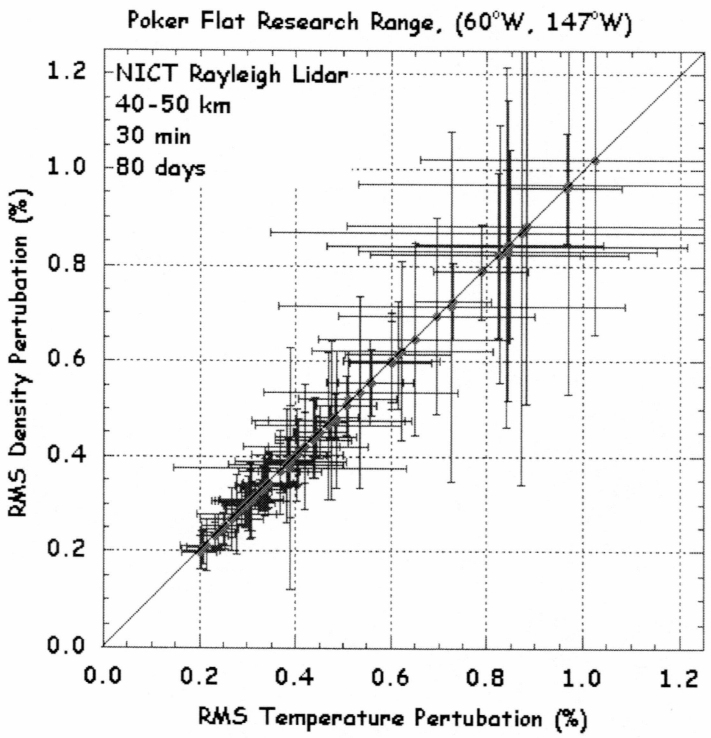

Figure 5.5: The rms signal amplitude of temperature plotted against density perturbations, for 30-min data for 80 sets of observations. The nights chosen are those, when the SNR is greater than one in both density and temperature perturbations. The uncertainty in rms amplitude estimation for each night is also plotted for temperature and density perturbations.

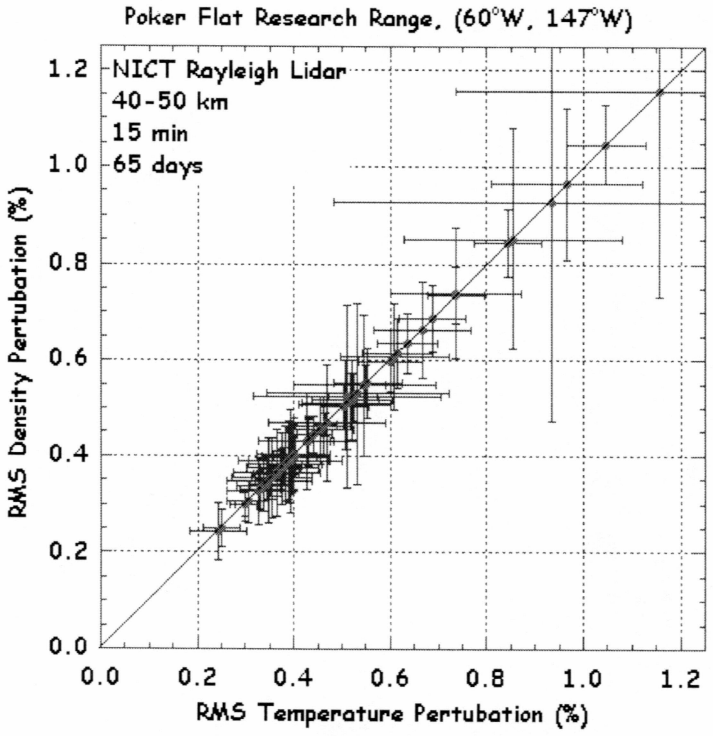

Figure 5.6: The rms signal amplitude of temperature plotted against density perturbations, for 15-min data for 65 sets of observations. The nights chosen are those, when the SNR is greater than one in both density and temperature perturbations. The uncertainty in rms amplitude estimation for each night is also plotted for temperature and density perturbations.

Chapter 6. Conclusions and Further Work

In this thesis we have presented a comprehensive study of the estimation of relative temperature perturbations and examined possible biases in the estimation of temperature fluctuations from Rayleigh lidar measurements. We have employed spectral analysis methods to examine the fluctuations and space-time series techniques to estimate the statistical properties of the signal power and noise power (i.e., their expected values and standard deviations).

We conclude that the estimate of the rms amplitude of the relative temperature perturbations does not vary significantly with the choice of the background temperature profile. We have analyzed the characteristics of the spatial periodogram (i.e., wavenumber spectrum) and autocorrelation functions of the relative temperature perturbation profiles. We see that the lidar signal is composed of a base-band geophysical signal and a white noise instrumental noise signal. We find that the noise power for measurements of different temporal resolution scale with the bandwidth of the measurements, indicating a white noise behavior in the temporal domain. Using spectral analysis, we determined the total power, the signal power, the noise power and the SNR. We have analyzed the uncertainties in the power estimates of the relative temperature profiles. We have determined the most robust method for calculating the signal and noise power using a combination of spectral and time-space series analysis. We find that as we increase the temporal resolution of the measurements and decrease the signal-to-noise ratio, the uncertainties in the power estimates increase. We also find that as altitude increases and the signal-to-noise ratio decrease, the uncertainties in the power estimates increase. This increase in uncertainty with altitude is reflected in both the geophysical and instrumental uncertainty. We compared the rms amplitudes of temperature and density perturbations for 89 nights of observations. We find that the geophysical power resulting from analysis of both the temperature and density perturbations are statistically

identical. The values of the rms amplitudes are similar to those reported from lidar studies in Greenland.

In this study, our goal has been to characterize the relative magnitude of the geophysical and instrumental variability in the lidar measurements and determine robust retrieval methods for studying the geophysical variability. We have not attempted to determine the causes and effects of the geophysical variability in the data. The effect of the seed initialization of temperature profiles at the highest altitude has not been studied explicitly. We appreciate that there are artifacts in the retrieval of temperature in the 70-80 km range. This study completes engineering analysis of the NICT-Rayleigh lidar measurements. The engineering analysis establishes a foundation for future geophysical studies of the gravity wave activity in the western Arctic.

References

Andrews, D. G., J. R. Holton, and C. B. Leovy, Middle atmosphere dynamics, Academic Press, Orlando, 1987.

Bevington, P. R., Data reduction and error analysis for the physical sciences, McGraw-Hill, New York, NY, 1969.

Bills, R. E., C. S. Gardner, and C.Y. She, Narrowband lidar technique for sodium temperature and Doppler wind observations of the upper atmosphere, Optical Engineering, 30, 13-21, 1991.

Brasseur, B., and S. Solomon, Aeronomy of the middle atmosphere, Reidel, Dordrecht, 1984.

Breese, J., Development of a Fe-Boltzmann temperature lidar, MS Thesis, University of Alaska, 2001.

Carlson, B. A., Communication systems an introduction to signals and noise in electrical communication, McGraw-Hill, 1986.

Chanin, M.L., Review of lidar contributions to the description and understanding of the middle atmosphere, Journal of Atmospheric and Terrestrial Physics, 46, 987-993, 1984.

Collins, R. L., and R. W. Smith, Evidence of damping and overturning of gravity waves in the Arctic mesosphere: Na lidar and OH temperature observations, Journal of Atmospheric and Solar-Terrestrial Physics, 66, 10, 2004.

Collins, R. L., M. C. Kelley, M. J. Nicolls, C. Ramos, T. Hou, T. E. Stern, K. Mizutani and T. Itabe, Simultaneous lidar observations of a noctilucent cloud and an internal wave in the polar mesosphere, Journal of Geophysical Research, 108, 8435-84311, 2003.

Collins, R L., D. Thorsen, and S. J. Franke, Comparative MF radar and and Na lidar measurements of fluctuating winds in the mesopause region, Journal of Geophysical Research, 14, 16583-16591, 1997.

Cutler, L. J., Rayleigh lidar studies of the arctic middle atmosphere, MS Thesis, University of Alaska, 2000.

Cutler, L. J., R. L. Collins, K. Mizutani, and T. Itabe, Rayleigh lidar observations of mesospheric inversion layers at Poker Flat, Alaska 65 °N, 147° W, Geophysical Research Letters, 28, 1467-1470, 2001.

Duck, T. J., J. A. Whiteway, and A. I. Carswell, A detailed record of High Arctic strato-mesospheric temperatures, Journal of Geophysical Research, in press to appear 2000.

Duck, T. J., J. A. Whiteway, and A. I. Carswell, Lidar observations of gravity wave activity and arctic stratospheric vortex core warming, Geophysical Research Letters, 25, 2813-2816, 1998.

Duck, T. J., and J. A. Whiteway, Seasonal transition in gravity wave activity during the springtime stratospheric vortex, Geophysical Research Letters, 27, 3477-3480, 2001.

Elterman, L., The measurement of stratospheric density distribution with the searchlight technique, Journal of Geophysical Research, 56, 509-520, 1951.

Fritts, D. C., and M. J. Alexander, Gravity dynamics and effects in the middle atmosphere, Rev. Geophys, 41, 1003, 2003.

Gerrard, A. J., and T. J. Kane, Synoptic scale study of the Arctic polar vortex's influence on the middle atmosphere, 1, Observations, Journal of Geophysical Research, 107, D16, ACL 1, 2002.

Gerrard, A. J., T. J. Kane, and J. P. Thayer, Noctilucent clouds and wave dynamics: Observations at Sondrestrom, Greenland, Geophysical Research Letters, 25, 2817-2820, 1998.

Gibbs, J. W. Fourier series, Nature, 59, 200 and 606, 1899.

Hauchecorne, A., M. L. Chanin, and R. Wilson, Mesospheric temperature inversion and gravity wave breaking, Geophysical Research Letters, 14, 933-936, 1987.

Hecht, J., The laser guidebook, McGraw-Hill, Inc., 1992.

Hedin, A.E., Extension of the MSIS Thermosphere Model into the Middle and Lower Atmosphere, Journal of Geophysical Research, 96, 1159, 1991. [http://nssdc.gsfc.nasa.gov/space/model/atmos/nrlmsise00.html]

Hines, C.O., Internal atmospheric gravity waves at ionospheric heights, Canadian Journal of Physics, 38, 1441-1481, 1960.

Hinkley, E.D., Laser Monitoring of the atmosphere, Springer-Verlag, New York, NY, 1976.

Holton, J. R., and M. J. Alexander, The role of waves in the transport circulation of the middle atmosphere, In Atmospheric science across the stratopause, D. E. Siskind, D. Eckermann, and M. E. Summers eds., Geophysical Monograph 123, 21-36, American Geophysical Union, Washington, 2000.

Hou, T., Development of high spectral resolution iron Boltzmann lidar, MS Thesis, University of Alaska, 2002.

Keckhut, P., A. Hauchecorne, and M. L. Chanin, Midlatitude long-term variability of the middle atmosphere: trends and cyclic and episodic changes, Journal of Geophysical Research, 100, 18,887-18,897, 1995.

Kent, G. S., and R.W. Wright, A review of laser radar measurements of atmospheric properties, Journal of Atmospheric and Terrestrial Physics, 32, 917-943, 1970.

Kong, J. A., Electromagnetic wave theory, Wiley and Sons, New York, NY, 1986.

Koopmans, L.H., Probability and mathematical statistics, the spectral analysis of time series, New York, NY, 1974.

Leblanc, T., and A. Hauchecorne, Recent observations of mesospheric temperature inversions, Journal of Geophysical Research, 102, 19471-19482, 1997.

Leblanc, T., I. S. McDermid, A. Hauchecorne, and P. Keckhut, Evaluation of optimization of lidar temperature analysis algorithms using simulated data, Journal of Geophysical Research, 103, 6177-6187, 1998.

Lord Rayleigh (J. W. Strutt), On the light from the sky, its polarization and colour, Phil. Mag., XLI, 107-120, 274-279, 1871.

Measures, R. M., Laser remote sensing fundamentals and applications, Kreiger, Malabar, FL, 1984.

Mitchell, N.J., L.Thomas, and A. K. P. Marsh, Lidar Studies of Strtospheric Gravity Waves: A Comparison of Analysis Techniques, Annales Geophysicae, 705-712, 8(10), 1990.

Mizutani, K., T. Itabe, M. Yasui, T. Aoki, Y. Murayama, and R. L. Collins, Rayleigh and Rayleigh doppler lidars for the observations of the arctic middle atmosphere, IEICE Transactions on Communications, vol. E83-B, no. 9, 2004-2009, September, 2000.

Oppenheim, A.V., A. S. Willsky, and I.T. Young, Signals and Systems, Prentice Hall, 1983.

Papoulis A., Probability, random variables, and stochastic processes, McGraw-Hill, New York, NY, 2002.

Press, S. A. Teukdsky, W. T. Vetterling, and B. P. Flannery, Numerical Recipies in FORTRAN: The art of scientific computing, Cambridge University Press, Cambridge, 1992.

Sears, F. W., University physics, Addison-Wesley, Reading, MA, 1965.

Silfvast, W. T., Laser fundamentals, Cambridge University Press, 1996.

Skoog, D. A., and J. J. Leary, Principles of instrumental analysis, Saunders College Publishing, Orlando, FL, 1992.

Solomon S., Stratospheric ozone depletion: A review of concepts and history, Reviews of Geophysical Letters, 37 (3), doi:10.1029/1999RG900008, 1999.

Sonwalkar, Vikas S., Notes on digital signal processing, Electrical and Computer Engineering Department, University of Alaska Fairbanks, 2001.

Stokes. G. G., On the dynamical theory of diffraction, Cambridge Phil Transactions, 7, 1-62, 1849.

Synge, E.H., A method of investigating the higher atmosphere, Phil. Magazine, 9, 1014-1020, 1930.

Wang, W., Spectral estimation of signal and noise power in Rayleigh lidar measurements of the middle atmosphere, MS Thesis, University of Alaska, 2003.

Wayne, R.P., Chemistry of atmospheres, Oxford University Press, 1985.

Whiteway, J.A., and Carswell, A.I., Rayleigh lidar observations of thermal structure and gravity wave activity in the High Arctic during a stratospheric warming, Journal of Atmospheric Sciences, 51, No.21,1994